Check for updates

Potent EGFR/PARP-1 inhibition by spirooxindole-triazole hybrids for targeted liver cancer therapy†

Mohamed S. Nafie, [ID] [ab] M. Ali, [ID] [c] Moayad Abdullah Alwehaibi,[c]
Abdulmajeed Abdullah Alayyaf,[c] Muhanna K. Al-Muhanna,[d] Naif S. Almuqati,[e]
Abdullah A. Alghamdi,[e] Matti Haukka, [ID] [f] Syeda Sumayya Tariq,[g] Zaheer Ul-Haq [ID] [g]
and Assem Barakat [ID] *[c]

The search for effective anti-cancer therapies has led to the exploration of dual inhibition strategies targeting multiple key molecular pathways. In this study, we aimed to design a novel candidate capable of dual inhibition targeting both EGFR (Epidermal Growth Factor Receptor) and PARP-1 (poly(ADP-ribose)polymerase-1), two crucial proteins implicated in cancer progression and resistance mechanisms. Through molecular hybridization and structure-based drug design approaches, we synthesized a series of compounds based on spirooxindole with triazole scaffolds with the potential for dual EGFR and PARP-1 inhibition. Interestingly, compounds **4a**, **4b** and **4f** showed potent cytotoxicity against HepG2 cells with IC_{50} values of 3.6, 4.6, and 1.9 μM compared to doxorubicin ($IC_{50} = 2.78$ μM), with poor cytotoxicity against THLE2 cells with IC_{50} values higher than 40 μM in a selective way. They exhibited potent EGFR and PARP-1 inhibition with IC_{50} values of 74.6, 85.3, and 116.1 nM compared to Erlotinib ($IC_{50} = 80$ nM, 94.7%). Additionally, they exhibited potent PARP-1 inhibition, with IC_{50} values of 2.01, 3.6, and 18.4 nM compared to Olaparib ($IC_{50} = 1.49$ nM, 94.5%). Furthermore, compound **4a**-treatment induced increased apoptosis by 6.6-fold, as the effective cell death mechanism. Overall, our study underscores the importance of multi-targeted approaches in developing effective anti-cancer agents.

1 Introduction

Numerous strategies have been approved for cancer treatment.[1] These strategies encompass the induction of apoptosis, the inhibition of signal transduction, the expression of gene modulators, and the suppression of angiogenesis.[2–4] In the first strategy, apoptosis induction targets and eliminates unwanted cancer cells while leaving healthy cells unaffected. Apoptosis

induction can be achieved by inhibiting or activating specific regulatory proteins, such as BAX, BCL-2, caspase-3, caspase-9, tubulin, and various kinases.[5] The upregulation of BAX and/or downregulation of BCL-2 have been documented as inducers of apoptotic cell death. Additionally, caspases, a group of protease enzymes, play a crucial role in enhancing apoptotic cell death. Among these, the initiator caspases (*e.g.*, caspase-9) and effector caspases (*e.g.*, caspase-3) are directly involved in the process of apoptosis.[5]

Another valuable strategy in cancer treatment involves the inhibition of the poly(ADP-ribose)polymerase (PARP) family of proteins.[6,7] Among the members of this family, PARP-1 is an adenosine diphosphate ribosyl transferase primarily localized within the nucleus and frequently associated with chromatin [8]. PARP-1 is an apoptosis-inducing factor that has been implicated in apoptotic cell death triggered by DNA damage. In recent years, significant research attention has been devoted to the development of PARP-1 inhibitors as potential antitumor drugs. PARP-1 plays a significant role in both the DNA repair process and the regulation of cell survival and death.[9,10] Numerous PARP-1 inhibitors, including Rucaparib[11] (Fig. 1), have been developed and utilized in clinical treatments. Typically, these inhibitors contain an amide fragment crucial for interacting with Ser904 and Gly863 residues, which are considered the key pharmacophore for PARP-1 inhibition. Many other

[a]Department of Chemistry, College of Sciences, University of Sharjah, Sharjah, 27272, United Arab Emirates. E-mail: mohamed.elsayed@sharjah.ac.ae

[b]Chemistry Department, Faculty of Science, Suez Canal University, Ismailia, 41522, Egypt. E-mail: mohamed_nafie@science.suez.edu.eg

[c]Department of Chemistry, College of Science, King Saud University, P. O. Box 2455, Riyadh 11451, Saudi Arabia. E-mail: mayyaf@ksu.edu.sa; Maly.c@ksu.edu.sa; 442105720@student.ksu.edu.sa; ambarakat@ksu.edu.sa

[d]The Material Science Research Institute, King Abdulaziz City for Science and Technology (KACST), Riyadh 11442, Saudi Arabia. E-mail: mmuhanna@kacst.edu.sa

[e]Refining and Petrochemical Technologies Institute (RPTI), KACST, Saudi Arabia

[f]Department of Chemistry, University of Jyväskylä, P.O. Box 35, FI-40014 Jyväskylä, Finland. E-mail: matti.o.haukka@jyu.fi

[g]Dr Panjwani Center for Molecular Medicine and Drug Research, International Center for Chemical and Biological Sciences, University of Karachi, Karachi-75270, Pakistan. E-mail: sumayyatariq7@gmail.com; zaheer_qasmi@hotmail.com

† Electronic supplementary information (ESI) available. CCDC 2360616–2360618. For ESI and crystallographic data in CIF or other electronic format see DOI: https://doi.org/10.1039/d4ra05966b
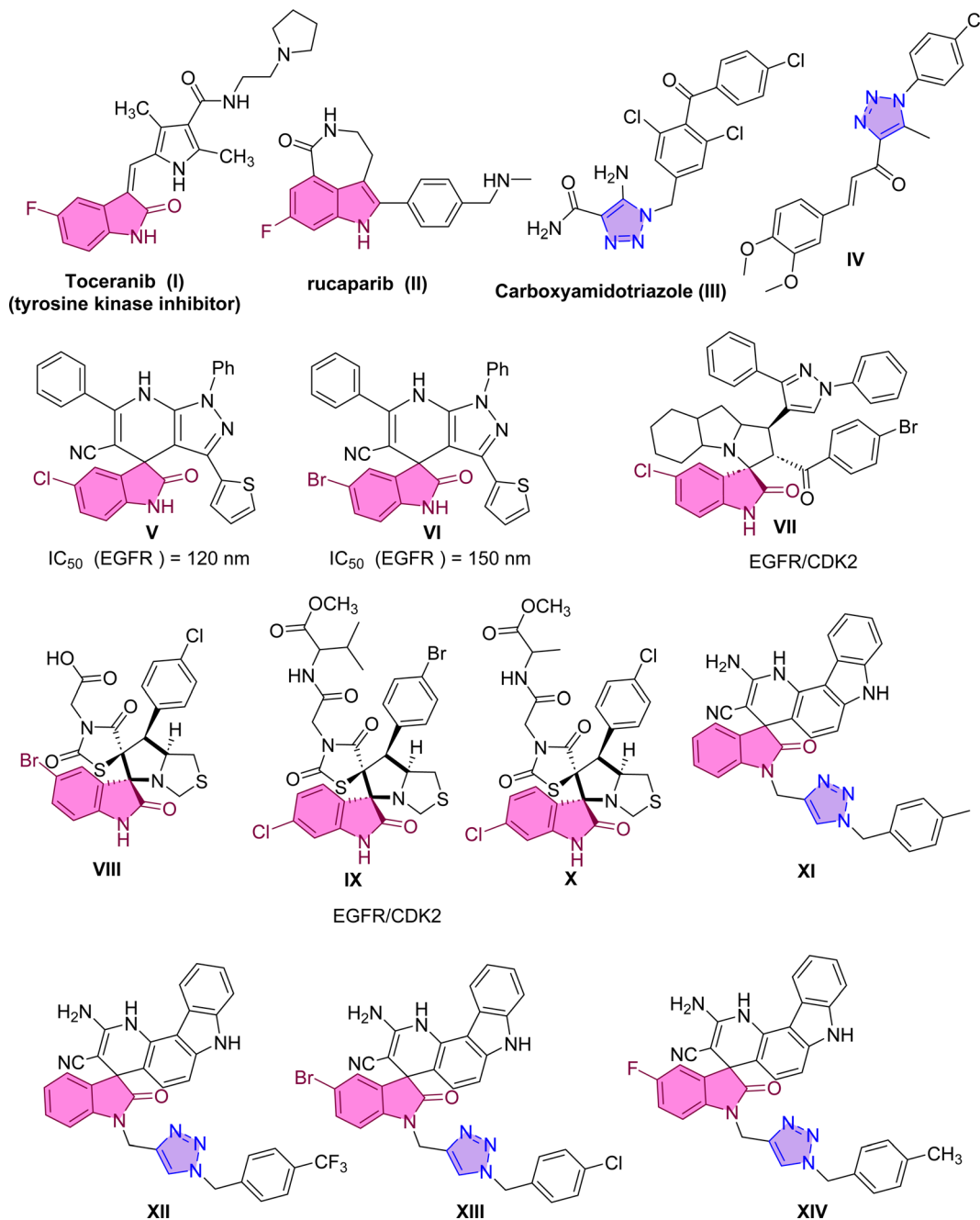
Fig. 1 Reported examples targeting EGFR and PARP-1 derived from spiro-heterocycles and triazole scaffold.

representative examples have been reported, either synthetically or naturally occurring, targeting the PARP-1 inhibition, such as chalcone-based triazole scaffold that exhibited apoptosis inducer and showed PARP-1 degrading activity.[12] Compound **IV** demonstrated potent inhibition of PARP-1 biosynthesis at a nanomolar concentration and exhibited an exceptional selectivity index.[13]

Due to its importance as a nitrogen heterocyclic compound, 1,2,3-triazole has found extensive use in constructing drug molecules,[14–16] particularly in the realm of anti-cancer agents.[17,18] Its chemical properties suggest that 1,2,3-triazole is an effective pharmacophore, facilitating interactions with drug receptors while maintaining favorable chemical and metabolic profiles.[19] Therefore, we retained the 1,2,3-triazole moiety to enhance the compound's activity.

Another alternative strategy for cancer treatment involves inhibiting a protein known as EGFR (Epidermal Growth Factor Receptor). The Epidermal Growth Factor Receptor (EGFR) represents a crucial molecular target in growth factor signaling.[20] Dysregulated signaling of these factors can result in uncontrolled cell proliferation, suppression of apoptosis, promotion of angiogenesis, facilitation of migration, and metastasis, all hallmark characteristics of cancer cells. The overexpression of EGFR in various human cancer cell types,

including liver, bladder, breast, colon, and lung cancer cells, has identified it as a promising molecular target for inhibition. Consequently, researchers have devised strategies to counteract the effects of EGFR activation, aiming to impede tumor growth and invasion. Various agents, such as specific antibodies targeting its ligand-binding domain and small molecules inhibiting its tyrosine kinase activity, are undergoing clinical trials or have already gained approval for clinical treatment. In 2018, Eldehna et al. reported the synthesis of spirooxindole derivatives V and VI through a one-pot three-component reaction.[21] These derivatives exhibited potent inhibition of EGFR, with IC_{50} values of 120 nM and 150 nM, respectively.[21]

A recent example in 2023, Al-Jassas et al. reported the design, synthesis, and evaluation of a series of spirooxindoles with pyrazole scaffold-targeted EGFR and CDK2 dual inhibitory effects. The spirooxindole hybrid VII displayed significant potential, with IC_{50} values of $0.189 \pm 0.01 \mu M$ (MCF-7) and $1.04 \pm 0.21 \mu M$ (HepG2). Furthermore, it possessed potent CDK-2 inhibition ($IC_{50} = 34.98$ nM) and an IC_{50} of 96.6 nM for EGFR inhibition.[22] Compound II also effectively regulated the expression of pro-apoptotic genes (P53, Bax, caspases-3, 8, and 9) while downregulating the anti-apoptotic gene BCL-2. In 2024, pyrrolidinyl-spirooxindole derivatives VIII–X were synthesized and found to possess dual activities against EGFR and CDK-2.[23] These compounds exhibited remarkable cytotoxicity against cancer cells, demonstrating notable potency against MCF-7 and MDA-MB-231 cells.

Molecular hybridization represents a novel approach to drug design and development. It involves combining pharmacophoric moieties from different bioactive substances to create a new hybrid compound. This hybridization aims to enhance the affinity and efficacy of the resulting compound compared to its parent drugs. A combination of triazole scaffold with spiro-heterocycles has demonstrated that compounds exhibit potent anti-cancer activities against cervical cancer HeLa cells. In a study by Sarkar et al., a series of chromenocarbazole tethered 1,2,3-triazoles were designed and synthesized using a click chemistry-based one-pot five-component reaction.[24] Compounds XI, XII, XIII, and XIV displayed excellent anti-proliferative activity (with IC_{50} values of 4.05, 3.54, 3.83, and 3.35 μM, respectively) in HeLa cells.

Based on these findings and the continuation of our research program about the development of the spirooxindole scaffold,[25–27] the aim of this study was to design a novel candidate capable of dual inhibition targeting both EGFR (Epidermal Growth Factor Receptor) and PARP-1 (poly(ADP-ribose) polymerase-1). In this text, we synthesized a series of spirooxindole hybrids with triazole scaffold, the compounds screened against two cancer cell lines (HepG2 and THLE2), and the most active candidate was further explored for mechanism of action targeting EGFR and PARP-1. Molecular docking study and molecular dynamic simulation were also explored.

2 Results and discussion

The synthesis of spirooxindole-triazole hybrids through [3 + 2] cycloaddition reactions offers a promising route for developing potent inhibitors targeting EGFR and PARP-1 for cancer therapy. The unique structure of these hybrids, combining the biological activities of spirooxindoles and 1,2,3-triazoles, is designed to enhance their therapeutic efficacy and specificity (Scheme 1). Isatin derivatives 2a–e, amino acid 3, and chalcone-based triazole scaffolds 1a–d were selected for their ability to form spirooxindole structures 4a–k in a one-step fashion. Azides were utilized to introduce the triazole ring via the [3 + 2] cycloaddition reaction with acetylacetone, forming an acetyl-triazole derivative, which was then employed as a precursor for synthesizing chalcone-based triazoles through aldol condensation with heteroaryl aldehydes followed our previously reported method. ^{1}H and ^{13}C-NMR spectroscopy were employed to confirm the chemical structure of the synthesized hybrids, identifying characteristic peaks corresponding to the oxindole, triazole, and other substituent groups. Single-crystal X-ray diffraction was successfully performed for acetyl-triazole derivative and two chalcone-based triazole compounds 1a and 1b, providing detailed information on their molecular geometry and crystal structure, and offering insights into the spatial arrangement of the hybrid molecules (Fig. 2). Compounds 4c and 4j serve as representative examples of the spirooxindole cycloadducts, whose chemical structures were confirmed through single-crystal X-ray analysis. These results have been published as a CSD Communication in 2024.[28,29] The data provide conclusive evidence of the absolute configuration and stereochemistry of the spirooxindole cycloadducts.
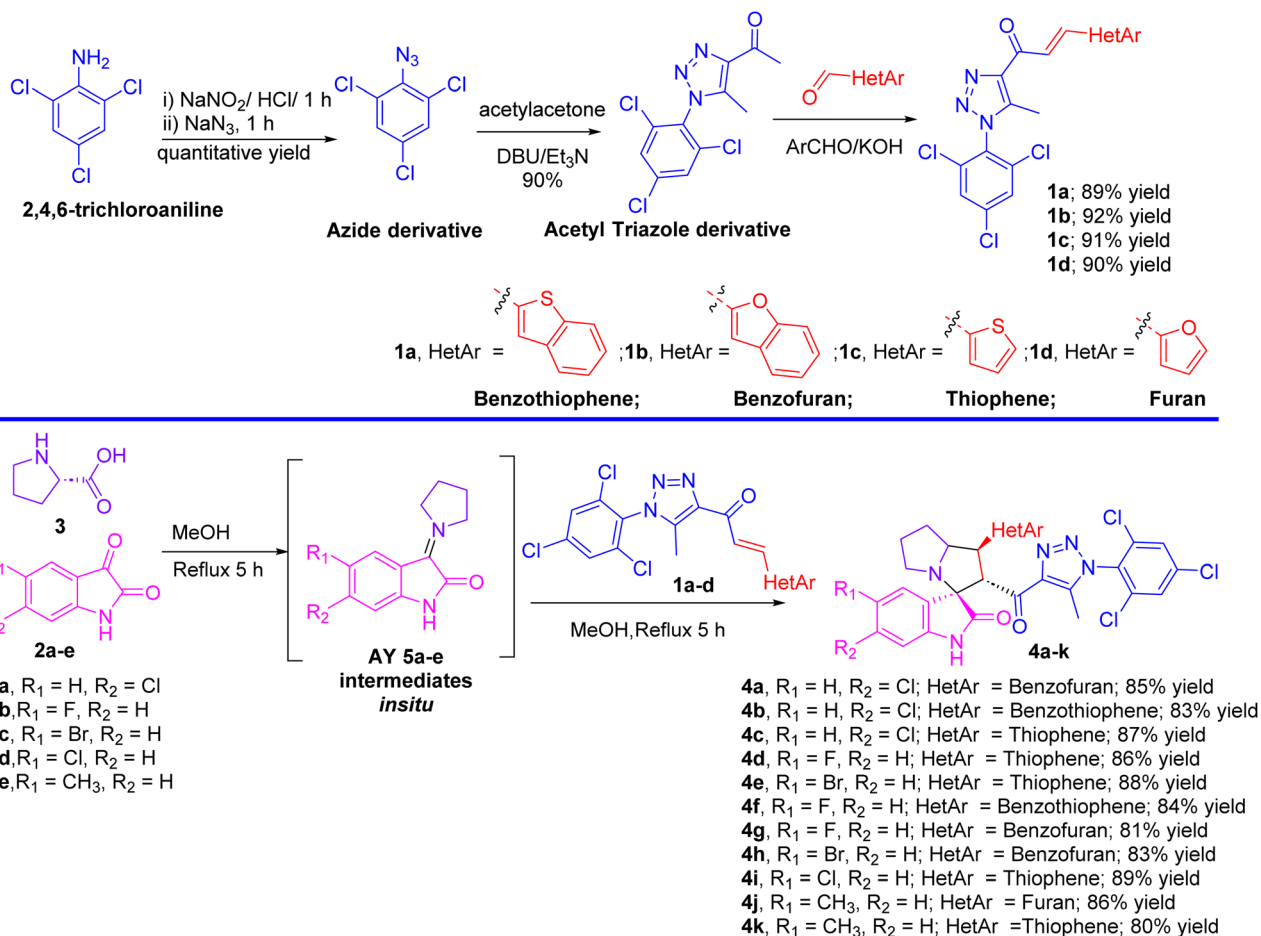
2.1 Cytotoxicity against cancer cells

The synthesized compounds were screened for their cytotoxicity against HepG2 and THLE2 cells using the MTT assay. As seen in Table 1, compounds 4a, 4b, and 4f showed potent cytotoxicity against HepG2 cells with IC_{50} values of 3.6, 4.6, and 1.9 μM compared to doxorubicin ($IC_{50} = 2.78$ μM), with poor cytotoxicity against THLE2 cells with IC_{50} values higher than 40 μM in a selective way. While compounds 1b, 1b, 1c, 4g, and 4h showed promising cytotoxicity against HepG2 cells with IC_{50} values range of 9.7–15.6 μM, with selective cytotoxicity against THLE2 cells with higher IC_{50} values. In contrast, other compounds weren't cytotoxic against HepG2 cells with higher IC_{50} values. Hence, compounds 4a, 4b, and 4f with potent cytotoxicity were examined for the EGFR/PARP-1 inhibition as the designed molecular targets.

2.2 EGFR/PARP-1 inhibition

Activity against EGFR and PARP-1 was assessed for compounds 4a, 4b, and 4f. It is worth noting, as shown in Table 2, they exhibited potent EGFR inhibition, with IC_{50} values of 74.6, 85.3, and 116.1 nM with the percentages of inhibition of 94.1%, 90.1%, 84.3% compared to Erlotinib ($IC_{50} = 80$ nM, 94.7%). Additionally, they exhibited potent PARP-1 inhibition, with IC_{50} values of 2.01, 3.6, and 18.4 nM with a percentage of inhibition of 95.2%, 81.2%, 86.6% compared to Olaparib ($IC_{50} = 1.49$ nM, 94.5%). The results show that inhibiting the EGFR/PARP-1 enzyme is a potential strategy that could explain the cytotoxic effects.

1a, HetAr = Benzothiophene; **1b**, HetAr = Benzofuran; **1c**, HetAr = Thiophene; **1d**, HetAr = Furan

2a, R$_1$ = H, R$_2$ = Cl
2b, R$_1$ = F, R$_2$ = H
2c, R$_1$ = Br, R$_2$ = H
2d, R$_1$ = Cl, R$_2$ = H
2e, R$_1$ = CH$_3$, R$_2$ = H

4a, R$_1$ = H, R$_2$ = Cl; HetAr = Benzofuran; 85% yield
4b, R$_1$ = H, R$_2$ = Cl; HetAr = Benzothiophene; 83% yield
4c, R$_1$ = H, R$_2$ = Cl; HetAr = Thiophene; 87% yield
4d, R$_1$ = F, R$_2$ = H; HetAr = Thiophene; 86% yield
4e, R$_1$ = Br, R$_2$ = H; HetAr = Thiophene; 88% yield
4f, R$_1$ = F, R$_2$ = H; HetAr = Benzothiophene; 84% yield
4g, R$_1$ = F, R$_2$ = H; HetAr = Benzofuran; 81% yield
4h, R$_1$ = Br, R$_2$ = H; HetAr = Benzofuran; 83% yield
4i, R$_1$ = Cl, R$_2$ = H; HetAr = Thiophene; 89% yield
4j, R$_1$ = CH$_3$, R$_2$ = H; HetAr = Furan; 86% yield
4k, R$_1$ = CH$_3$, R$_2$ = H; HetAr = Thiophene; 80% yield

Scheme 1 Synthesis of the spirooxindoles **4a–k**.
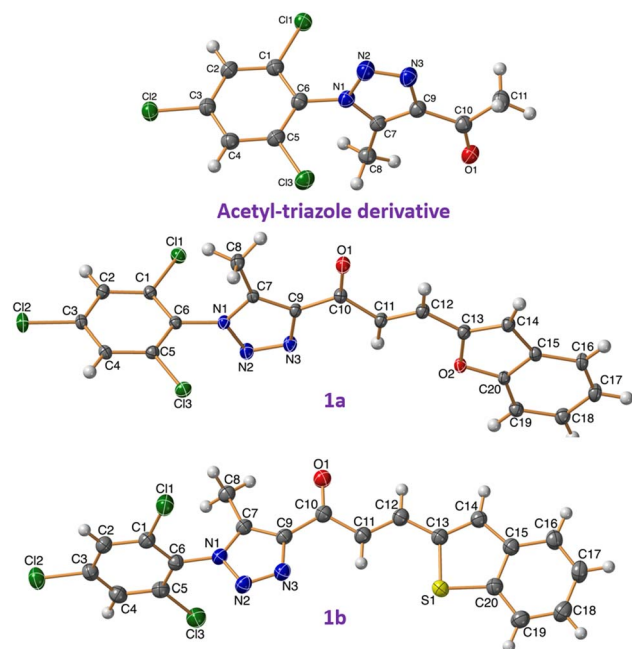
Fig. 2 X-ray for the chalcones based triazole scaffold acetyl-triazole derivative and chalcones **1a** and **1b**.

The spirooxindole triazole compound is an effective treatment for liver cancer due to its ability to block growth factors from activating the EGFR receptor, preventing tumor growth. This bidirectional action targets both the tumor and immune system, enhancing the body's ability to fight cancer. In early experiments, the compound significantly reduced liver cancer tumors and increased survival rates compared to untreated mice. It also increased apoptosis and decreased cell growth, demonstrating its effectiveness against cancer cells in multiple ways.

The spirooxindole triazole compound inhibits the growth of cancer cells. It accomplishes this by focusing on and inhibiting PARP-1, a protein. Cancer cells cannot repair DNA damage if PARP-1 is inhibited, leading to more DNA damage and, ultimately, cell death. The chemical kills cancer cells by targeting PARP-1, which prevents them from repairing themselves. Because it inhibits tumor growth and enhances the immune system's response, the spirooxindole triazole molecule represents an encouraging prospect for cancer treatment. The chemical spirooxindole triazole was utilized in a preclinical investigation; it inhibited PARP-1 and led to DNA damage accumulation in cancer cells. As a result, tumor development in mice was significantly reduced. Additionally, the chemical

Table 1 The results of MTT assay and determination of the cytotoxicity for the synthesized compounds against HepG2 and THLE2 cells[a]
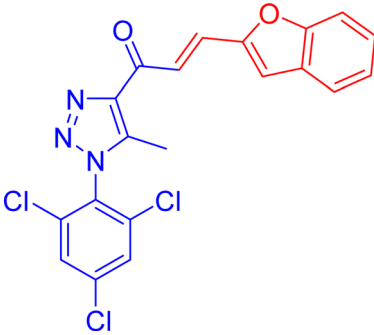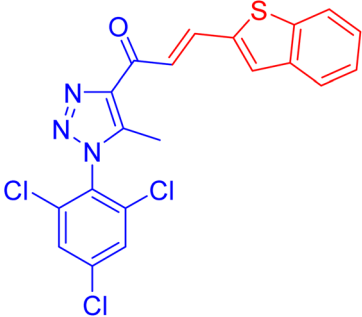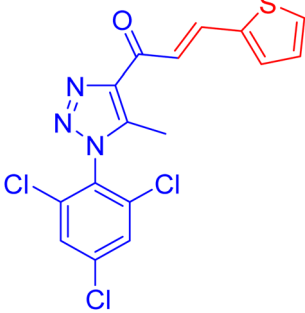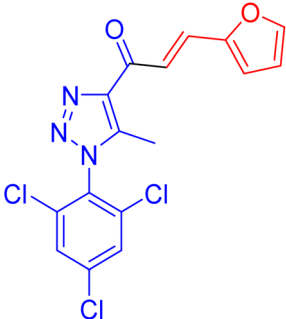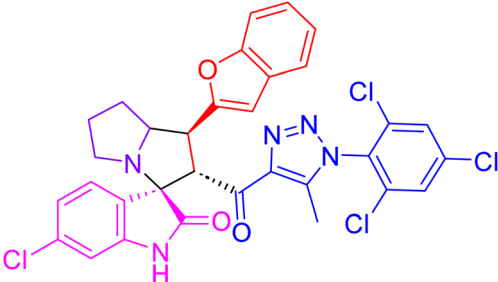
#	Chemical structures	IC$_{50}$ ± SD [µM]	
		HepG2	THLE2
1a		9.7 ± 0.2	45.8 ± 2.1
1b		8.5 ± 0.4	42.9 ± 3.0
1c		16.8 ± 0.5	32.5 ± 1.9
1d		17.6 ± 0.4	42.3 ± 0.9
4a		3.6 ± 0.1	43.8 ± 2.9
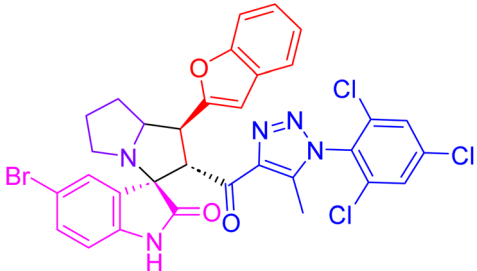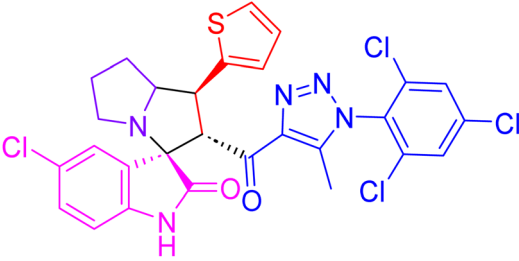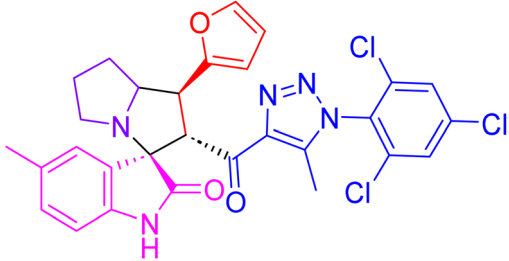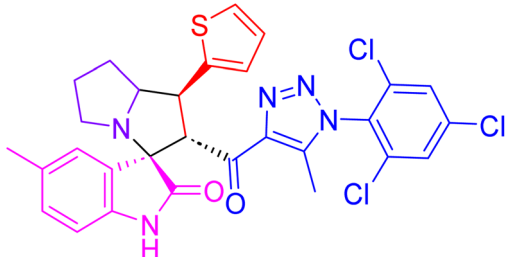
Table 1 (*Contd.*)

#	Chemical structures	IC$_{50}$ ± SD [μM]	
		HepG2	THLE2
4b		4.6 ± 0.2	39.8 ± 2.0
4c		27.3 ± 0.9	NT
4d		31.5 ± 1.5	NT
4e		28.9 ± 1.1	NT
4f		1.9 ± 0.1	43.7
4g		8.9 ± 0.3	38.4 ± 1.6

RSC Advances

Table 1 (*Contd.*)

#	Chemical structures	IC$_{50}$ ± SD [µM]	
		HepG2	THLE2
4h		15.6 ± 0.4	29.7 ± 1.2
4i		38.9 ± 1.4	NT
4j		14.3 ± 0.7	39.0 ± 2.3
4k		37.5 ± 1.7	NT

[a] Values are expressed as mean ± SD of three independent trials. NT = non-tested. IC$_{50}$ of doxorubicin (DOX) = 2.78 µM as a reference drug.

improved the efficacy of immune checkpoint inhibitors, which accelerated tumor regression and improved immune responses to malignancies.

2.3 Apoptosis-investigation activity

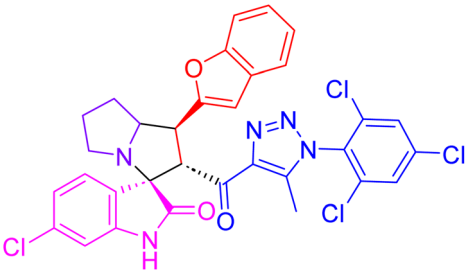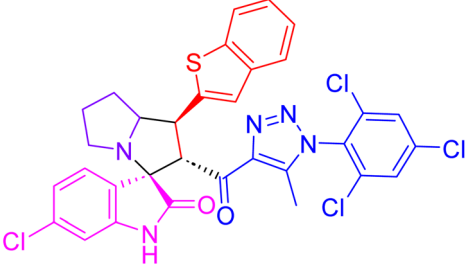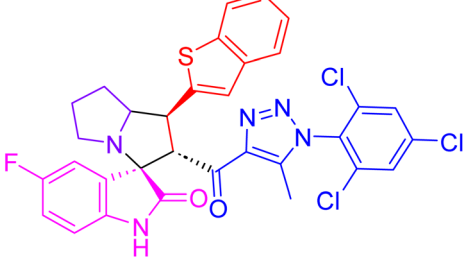#### 2.3.1 Apoptotic investigation

2.3.1.1 Annexin V/PI staining with cell cycle analysis. Flow cytometric examination of Annexin V/PI staining of both untreated and **4a**-treated HepG2 cells was used to investigate the apoptotic activity of compound **4a**. Fig. 3(A) showed that compound **4a** activated apoptotic cell death, increasing the cell

population in total apoptosis by 13.05% (0.95% late and 12.1% early apoptosis) compared to the untreated group (1.97%). While, it didn't affect necrotic cell death, as it reduced cells in necrosis by 0.58% compared to 0.61% in the untreated control. Hence, compound **4a**-treatment induced apoptosis by 6.62-fold.

Additionally, As can be shown in Fig. 3(B), the cell population in the "G2/M-phase" was significantly increased by 42% after treatment with compound **4a**, compared to the control 34%, whereas the cell population in the "S-phase" was non-significantly increased by 33% after treatment compared to

Table 2 IC$_{50}$ values of EGFR and PARP-1 kinase activities of the tested compounds[a]

≠	Chemical structure	IC$_{50}$ ± SD [nM]	
		EGFR	PARP-1
4a		74.6 ± 1.8	2.01 ± 0.1
4b		85.3 ± 2.9	3.6 ± 0.3
4f		116.1 ± 3.1	18.4 ± 1.0
Erlotinib		80.1 ± 1.8 (ref. 30)	—
Olaparib		—	1.49 ± 0.2 (ref. 31)

[a] "Values are expressed as an average of three independent replicates". "IC$_{50}$ values were calculated using sigmoidal non-linear regression curve fit of percentage inhibition against five concentrations of each compound".

the control 30%, hence, in contrast, cells population at "G0–G1-phase" were decreased upon treatment.

2.4 Gene expression analysis of apoptosis-related genes

To confirm apoptotic cell death, RT-PCR was used on both the untreated and treated HepG2 cells (Fig. 4). The expression of pro-apoptotic genes "P53, Bax, and caspases 3, 8, and 9" was upregulated by **4a** treatment, corresponding fold changes of 9.3, 4.6, 5.6, 3.5, and 8.6, respectively. Concurrently, it resulted in a 0.37-fold decrease in the gene expression of the anti-apoptotic BCL-2. These findings align with the possibility of triggering cell death by blocking enzymes. The release of "cytochrome c" and loss of mitochondrial potential are the results of activation of the intrinsic pathway of apoptosis. Cell death occurring through "caspase-dependent apoptosis" occurs when the ratio of proteins that promote cell death to those that prevent it

increases, setting in motion a cascade reaction involving activations of caspases 3 and 9 proteins.

In accordance with previous literature,[32–34] both molecular targets of EGFR and PARP-1, which target tumor growth and resistance to conventional therapies, hold great promise as a liver cancer treatment option. Researchers aim to inhibit these critical processes, potentially improving the efficacy of radiation therapy and chemotherapy. This approach may be the last resort for patients who have not responded to standard therapies or cannot undergo surgery. A synergistic impact between PARP-1 and EGFR medicines could improve outcomes and survival rates for liver cancer patients. Preclinical studies have shown promising results with the potential to revolutionize future treatments. A mouse model will be further recommended to validate the decrease of tumor size after therapy targeting angiogenesis and immunological checkpoint pathways. This two-pronged approach may circumvent the limitations of
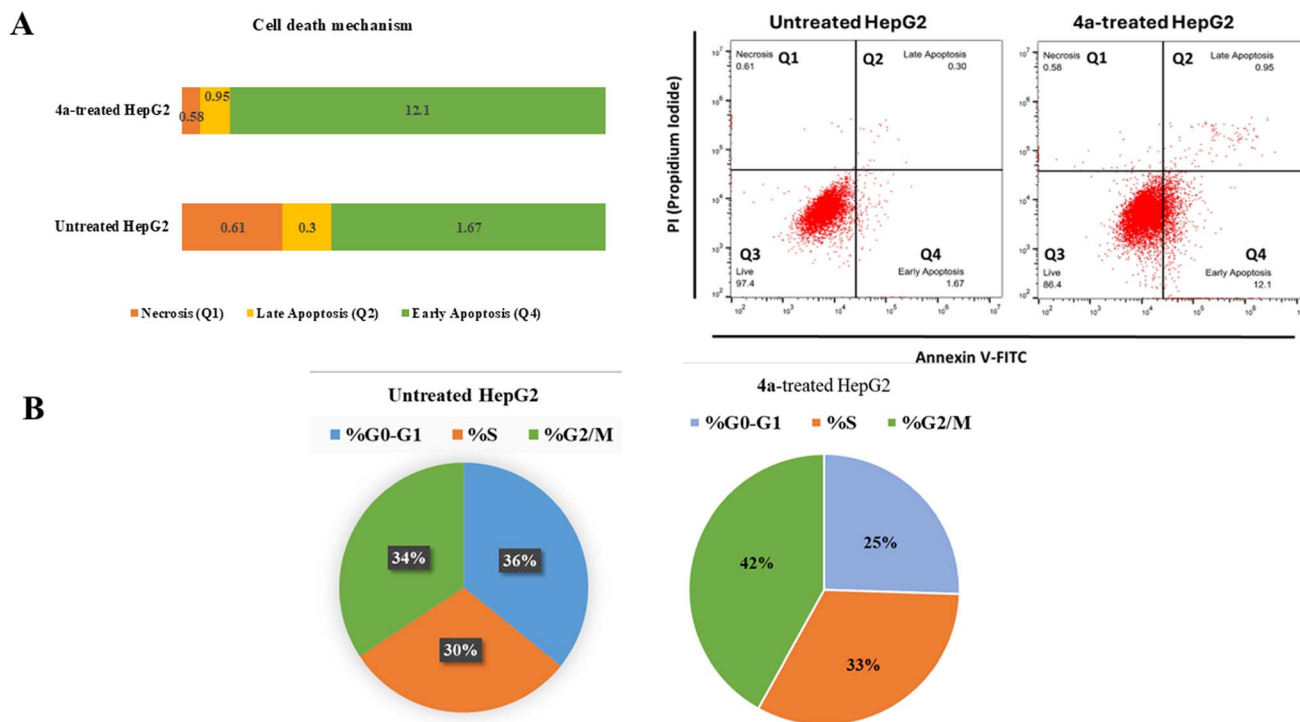
A

Fig. 3 (A) Pie-chart representation of the percentage of apoptosis (early and late apoptotic cell population) using Annexin V/propidium iodide staining. (B) Pie-chart representation of the percentage of cell population at each cell phase in untreated and **4a**-treated HepG2 cells, with the IC$_{50}$ value at 48 h. "The data shown are the average of three independent experimental runs (mean ± SD)".
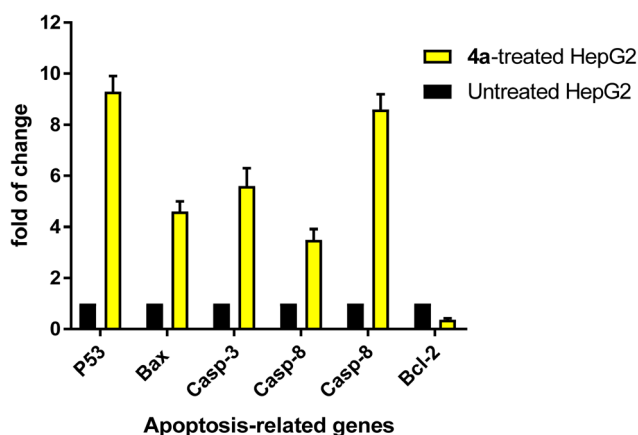

Fig. 4 Gene expression levels of apoptosis-related genes of untreated and **4a**-treated HepG2 cells with the IC$_{50}$ value. "Values are expressed as mean ± SD of three independent replicates". "Data were normalized using β-actin as a housekeeping gene". "The dashed line represents the gene expression level of untreated control. Fold change was calculated using $2^{-\Delta\Delta CT}$".

current therapies and provide a more tailored a future chance of treatment for liver cancer.

2.5 Molecular interactions

Molecular docking was used for the evaluation of the binding modes of the spirotriazole derivatives against poly(ADP-ribose) polymerase (PARP1) and Epidermal Growth Factor Receptor (EGFR). For this purpose, the crystal structure of PDB IDs 7AAD and 1M17, respectively. The respective controls Olaparib and Erlotinib were also subjected to docking along with the spiro-triazole derivatives.

Analysis of the PARP1–ligand (**4a**) complex with the best IC$_{50}$ (compound **4a**) and top-ranked pose *via* Protein–Ligand Interaction Profiler (PLIP) revealed Hydrogen bonding with Asp766 and Tyr896 residues of the PARP1 at a bond distance of 1.93 and 2.89 Å respectively, while residues Ile872, Leu877, Arg878, Tyr889, Ala898, and Glu988 were found to be involved in hydrophobic interactions. Similarly, the PLIP analysis of the PARP-Olaparib complex revealed Gly863, Ser864, and Ser904 forming hydrogen bonds with Olaparib at a distance of 2.10, 1.76, and 1.85 Å, respectively, while Glu763, Arg878, Tyr896, Tyr907, Glu988 were found involved in hydrophobic bonding. Fig. 5 shows the molecular interactions within (A) PARP1–ligand and (B) PARP1–control.

In case of EGFR, analysis of the EGFR–ligand (**4a**) complex with the best IC$_{50}$ and top-ranked pose *via* Protein–Ligand Interaction Profiler (PLIP) revealed hydrogen bonding with Arg817 at a distance of 2.25 Å while residues Leu694, and Phe699 took part in hydrophobic bonding with the ligand. On comparison with the EGFR–Erlotinib complex, it was found that this interaction involved hydrogen bonding *via* Ser696, in addition to Lys721, Thr766, and Met769 at a distance of 3.35, 3.30, 3.16, and 2.63 Å, respectively. Residues Leu694, Val702, Leu768, and Leu820 were found involved in hydrophobic
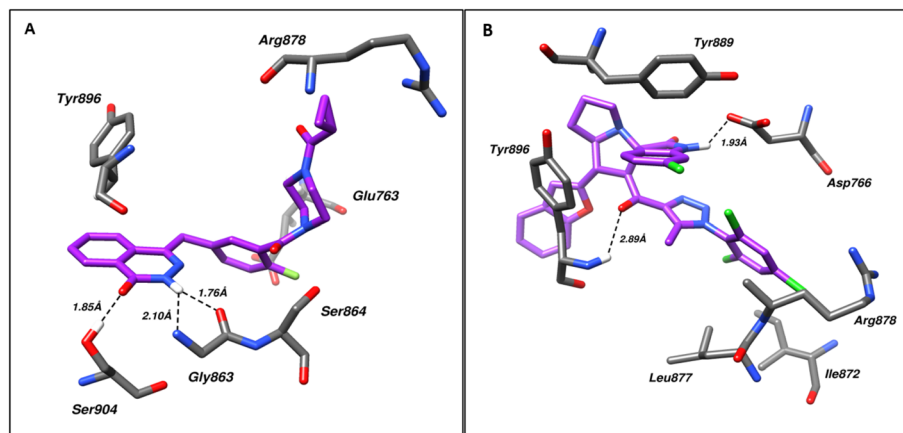
Fig. 5 Shows the molecular interactions within (A) PARP1–control and (B) PARP1–ligand (**4a**). Hydrogen bonds are shown as dotted lines.

bonding. Fig. 6 shows the molecular interactions within (A) EGFR–ligand and (B) EGFR–control.

2.6 Molecular dynamics

To assess the structural stability of the protein–ligand complex, RMSDs of the 50 ns simulated trajectories were calculated. The RMSD of any simulated biomolecular system serves as an essential parameter to gauge the system's stability. In the context of structural biology, when studying the atomic coordinates, the lower RMSD values indicate greater system stability, whereas larger RMSD values correspond to less stable complexes.[35] Throughout the simulation, both the PARP1 and EGFR exhibited consistent RMSDs with minimal fluctuations, indicating that the complexes remained stable throughout the simulation.

In order to assess the inherent flexibility of the protein during the simulation run, Root Mean Square Fluctuations (RMSF) of the simulated trajectories, were computed. The RMSF provides information regarding residue-level perturbations where higher values within a biomolecular system signify flexibility and, consequently a less stable state.[36] On the other hand, reduced fluctuation imparts greater stability to the system.[37]
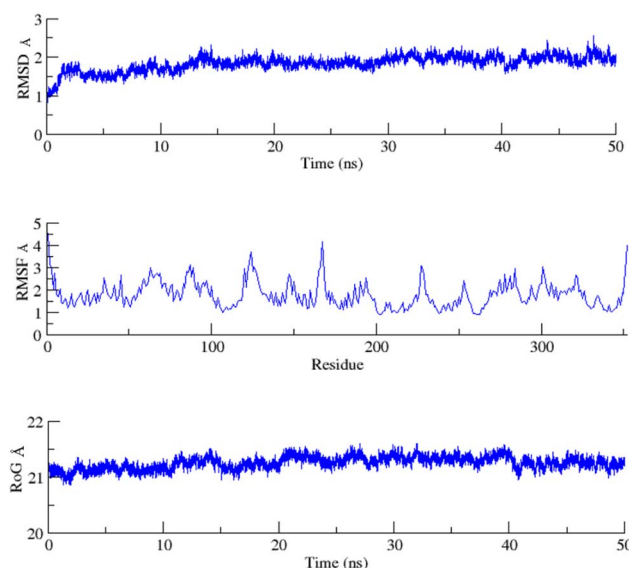

Fig. 7 RMSD, RMSF and RoG plots of the PARP1 systems calculated as a function of time.
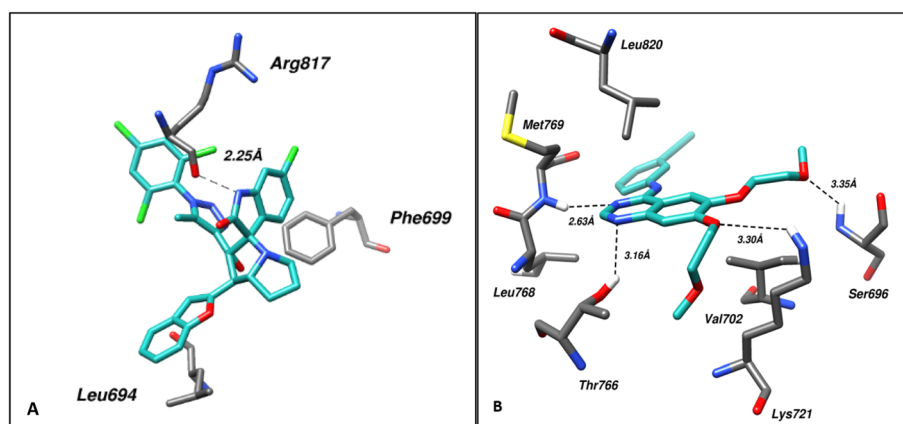

Fig. 6 Shows the molecular interactions within (A) EGFR–ligand (**4a**) and (B) EGFR–control. Hydrogen bonds are shown as dotted lines.
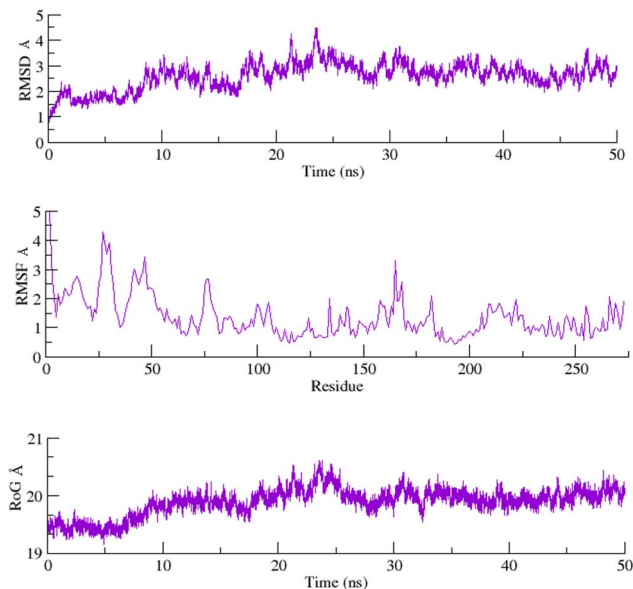
Fig. 8 RMSD, RMSF and RoG plots of the EGFR systems calculated as a function of time.

The average RMSFs recorded for PARP1 and EGFR, indicated that the protein residues remained stable upon interaction.

The structural properties of the simulated ensembles were further assessed *via* the time-dependent convergence of the radius of gyration (RoG), which is related to the compactness of the protein. A properly folded conformation in general features constant gyration values, while on the other hand, distortion in the folding behavior induces the RoG values to change over time.[38] The average RoG recorded for the PARP–ligand and EGFR–ligand complexes demonstrated stability with minimal fluctuations. The RMSD, RMSF, and RoG plots of the PARP1 and EGFR systems are shown in Fig. 7 and 8 respectively.

3 Materials and methods

3.1 Synthesis of 1-(5-methyl-1-(2,4,6-trichlorophenyl)-1*H*-1,2,3-triazol-4-yl)ethan-1-one 1

To a stirring solution of 2,4,6-trichloroaniline (6.05 g, 0.0308 mol) in dil. HCl (40 mL, 3 M). A solution of sodium nitrite (2.34 g, 0.0339 mol, 25 mL, 1 M) is treated at temperature <10 °C. The progress of the reaction is confirmed by liberation of brown gases (1 h). When the brown gases crases a solution of sodium azide (4.006 g, 0.0616 mol) is added to the stirring cold reaction mass. The formation of product is confirmed by TLC (1 h). The reaction mixture was extracted using diethylether. A brown viscous liquid confirmed the product **1**.

A solution of the appropriate azide (10.0 mmol, 2.22 gm) and acetylacetone (2.0 g, 20.0 mmol) in CHCl$_3$ (20 mL) was treated by adding Et$_3$N (2.02 g, 20.0 mmol) and DBU (0.76 g, 5.00 mmol). The reaction mixture was stirred at room temperature for 1–2 h. The solvent was removed, and water is added then extracted with Et$_2$O, dried with Na$_2$SO$_4$, evaporated and the solid product was washed with the *n*-hexane to provide pure compound.

^{1}H NMR (500 MHz, DMSO-d_6) δ 8.14 (s, 2H), 2.66 (s, 3H), 2.68–2.62 (m, 1H), 2.37 (s, 3H); ^{13}C NMR (126 MHz, DMSO-d_6) δ 193.55, 142.99, 140.00, 138.09, 134.38, 130.07, 129.66, 28.15, 8.99; m.p: 131 °C; powder.

3.2 General method for the synthesis of the chalcones based triazole 1a–d (GP1)

A mixture of heteroaryle aldehyde (2 mmol) and 1-(5-methyl-1-(2,4,6-trichlorophenyl)-1*H*-1,2,3-triazol-4-yl)ethan-1-one (0.609 g, 2.0 mmol) dissolved in ethanol (20 mL) was added slowly to an aqueous solution of potassium hydroxide (2.0 mmol, 112 mg) in water (10 mL). The mixture was stirred in crushed-ice bath for 2 h, stirred at 20–25 °C for 4 h. The mixture was filtrated and the residue was washed with cold water and cold alcohol dried to give the titled compound without further purification.

3.2.1 (*E*)-3-(Benzofuran-2-yl)-1-(5-methyl-1-(2,4,6-trichlorophenyl)-1*H*-1,2,3-triazol-4-yl)prop-2-en-1-one 1a. Benzofuran-2-carbaldehyde (2 mmol, 292 mg) was used according to the general procedure GP1 to afford the desired chalcone **1a**. m.p: 101–103 °C; yellow powder. ^{1}H NMR (400 MHz, CDCl$_3$) δ 8.18 (d, *J* = 15.6 Hz, 1H), 7.84 (d, *J* = 15.9 Hz, 1H), 7.61–7.51 (m, 4H), 7.43–7.33 (t, *J* = 7.44 Hz, 1H), 7.26–7.22 (t, *J* = 8.32 Hz, 1H), 7.08 (s, 1H), 2.51 (s, 3H); ^{13}C NMR (101 MHz, CDCl$_3$) δ 183.83, 155.87, 153.26, 143.49, 140.72, 138.19, 135.14, 130.41, 130.04, 129.25, 129.21, 129.17, 128.64, 126.89, 123.49, 121.92, 112.71, 112.64, 111.71, 9.25.

3.2.2 (*E*)-3-(Benzo[*b*]thiophen-2-yl)-1-(5-methyl-1-(2,4,6-trichlorophenyl)-1*H*-1,2,3-triazol-4-yl)prop-2-en-1-one 1b. Benzothiophene-2-carbaldehyde (2 mmol, 324 mg) was used according to the general procedure GP1 to afford the desired chalcone **1b**. m.p: 90–92 °C; yellow powder. ^{1}H NMR (400 MHz, CDCl$_3$) δ 8.16 (d, *J* = 15.7 Hz, 1H), 7.91 (d, *J* = 15.4 Hz, 1H), 7.83–7.77 (m, 2H), 7.61 (s, 1H), 7.57 (s, 2H), 7.39–7.33 (m, 2H), 2.50 (s, 3H); ^{13}C NMR (101 MHz, CDCl$_3$) δ 183.63, 143.39, 140.78, 140.73, 140.59, 139.77, 138.20, 137.11, 135.13, 130.23, 130.14, 130.03, 129.27, 129.17, 126.53, 124.99, 124.65, 124.58, 124.17, 122.66, 9.31, 9.24.

Chalcones **1c** and **1d** was prepared according our prevous published article.[39]

3.3 General method for the synthesis of spirooxindoles triazole hybrids 4a–k (GP2)

A mixture of the chalcones **1a–d** (0.5 mmol), isatin derivatives (0.5 mmol) and ʟ-proline (57.5 mg, 0.5 mmol) in methanol (10 mL) was refluxed on oil bath for appropriate time 5–8 h. After completion of the reaction as evident from TLC, the reaction was kept at room temperature overnight and the solid precipitated upon slow evaporation was filtered off without any further purification.

3.3.1 (1′*S*,2′*S*,3*R*)-1′-(Benzofuran-2-yl)-6-chloro-2′-(5-methyl-1-(2,4,6-trichlorophenyl)-1*H*-1,2,3-triazole-4-carbonyl)-1′,2′,5′,6′,7′,7*a*′-hexahydrospiro[indoline-3,3′-pyrrolizin]-2-one 4a. The chalcone **1a** (215.5 mg, 0.5 mmol), 6-clisatin **2a** (90.5 mg, 0.5 mmol) was used according to the general procedure GP2 to afford the spirooxindoles triazole hybrid **4a**. m.p:

180–182 °C; yellow crystal; 85% yield. $[\alpha]_{25}^{\lambda}$ = +28.060 (c 0.01, MeOH); (TLC: 50% *n*-hexane/EtOAc; R_f = 0.8); ^{1}H NMR (400 MHz, DMSO-d_6) δ 10.63 (s, 1*H*), 8.09 (d, *J* = 2.2 Hz, 1H), 8.05 (d, *J* = 2.2 Hz, 1H), 7.92 (d, *J* = 7.7 Hz, 1H), 7.79 (d, *J* = 7.5 Hz, 1H), 7.39 (s, 1H), 7.35–7.27 (dt, *J* = 18.9, 7.1 Hz, 2H), 7.07 (d, *J* = 7.9 Hz, 1H), 6.87 (dd, *J* = 8.0, 2.1 Hz, 1H), 6.60 (d, *J* = 2.1 Hz, 1H), 5.00 (d, *J* = 10.3 Hz, 1H), 4.26 (d, *J* = 6.4 Hz, 2H), 2.92–2.86 (m, 1H), 2.51–2.37 (m, 2H), 2.06 (s, 3H), 2.01–1.69 (m, 3H); ^{13}C NMR (101 MHz, DMSO-d_6) δ 192.27, 179.83, 179.76, 144.93, 142.58, 140.50, 140.45, 140.10, 139.00, 138.20, 134.38, 134.22, 130.83, 129.55, 129.34, 124.40, 121.62, 109.21, 71.64, 9.10, 7.92; LC/MS (ESI, *m/z*): found 666.11 [M(^{35}Cl) + H]$^+$, 668.17 [M(^{37}Cl) + H]$^+$, exact mass 667.37 for $C_{32}H_{23}Cl_4N_5O_3$; elemental analysis: C, 57.59; H, 3.47; N, 10.49; found C, 57.60; H, 3.48; N, 10.51.

3.3.2 (1′S,2′S,3R)-1′-(Benzo[*b*]thiophen-2-yl)-6-chloro-2′-(5-methyl-1-(2,4,6-trichlorophenyl)-1*H*-1,2,3-triazole-4-carbonyl)-1′,2′,5′,6′,7′,7a′-hexahydrospiro[indoline-3,3′-pyrrolizin]-2-one 4b.

The chalcone **1b** (223.5 mg, 0.5 mmol), 6-Cl-isatin **2a** (90.5 mg, 0.5 mmol) was used according to the general procedure GP2 to afford the spirooxindoles triazole hybrid **4b**. m.p: 183–185 °C; white crystal; 83% yield. $[\alpha]_{25}^{\lambda}$ = +22.541 (c 0.01, MeOH); (TLC: 50% *n*-hexane/EtOAc; R_f = 0.825); ^{1}H NMR (400 MHz, DMSO-d_6) δ 10.63 (s, 1H), 8.09 (d, *J* = 2.2 Hz, 1H), 8.05 (d, *J* = 2.2 Hz, 1H), 7.91 (d, *J* = 7.7 Hz, 1H), 7.79 (d, *J* = 7.5 Hz, 1H), 7.39 (s, 1H), 7.32 (dt, *J* = 18.9, 7.1 Hz, 2H), 7.06 (d, *J* = 7.9 Hz, 1H), 6.86 (dd, *J* = 8.0, 2.1 Hz, 1H), 6.60 (d, *J* = 2.1 Hz, 1H), 5.00 (d, *J* = 10.3 Hz, 1H), 4.26 (d, *J* = 6.4 Hz, 2H), 2.95–2.84 (m, 1H), 2.50–2.35 (m, 2H), 2.06 (s, 3H), 2.01–1.69 (m, 3H); ^{13}C NMR (101 MHz, DMSO-d_6) δ 192.27, 179.83, 179.76, 144.93, 142.58, 140.50, 140.45, 140.10, 139.00, 138.20, 134.38, 134.22, 130.83, 129.55, 129.34, 124.40, 121.62, 109.21, 71.64, 9.10, 7.92; LC/MS (ESI, *m/z*): found 682.14 [M(^{35}Cl) + H]$^+$, 684.13 [M(^{37}Cl) + H]$^+$, exact mass 683.43 for $C_{32}H_{23}Cl_4N_5O_2S$; elemental analysis: C, 56.24; H, 3.39; N, 10.25; found C, 56.23; H, 3.38; N, 10.22.

3.3.3 (1′S,2′S,3R)-6-Chloro-2′-(5-methyl-1-(2,4,6-tri-chlorophenyl)-1*H*-1,2,3-triazole-4-carbonyl)-1′-(thiophen-2-yl)-1′,2′,5′,6′,7′,7a′-hexahydrospiro[indoline-3,3′-pyrrolizin]-2-one 4c.

The chalcone **1c** (198.5 mg, 0.5 mmol), 6-Clisatin **2a** (90.5 mg, 0.5 mmol) was used according to the general procedure GP2 to afford the spirooxindoles triazole hybrid **4c**. m.p: 155–157 °C; white crystal; 87% yield. $[\alpha]_{25}^{\lambda}$ = +60.408 (c 0.01, MeOH); (TLC: 50% *n*-hexane/EtOAc; R_f = 0.775); ^{1}H NMR (400 MHz, DMSO-d_6) δ 10.62 (s, 1H), 8.12–8.04 (m, 1H), 7.41 (d, *J* = 4.9 Hz, 1H), 7.09–6.98 (m, 2H), 6.99 (d, *J* = 4.4 Hz, 1H), 6.86 (d, *J* = 8.1 Hz, 1H), 6.59 (s, 1H), 4.89 (d, *J* = 10.1 Hz, 1H), 4.20 (d, *J* = 10.3 Hz, 1H), 4.16 (s, 1H), 2.89 (d, *J* = 8.3 Hz, 1H), 2.07 (d, *J* = 12.5 Hz, 4H), 2.04 (s, 1H), 2.05–1.90 (m, 2H), 1.88–1.68 (m, 2H); ^{13}C NMR (100 MHz, DMSO-d_6) δ 144.90, 142.60, 140.42, 138.19, 134.39, 130.89, 129.35, 121.66, 7.89. LC/MS (ESI, *m/z*): found 632.06 [M(^{35}Cl) + H]$^+$, 634.08 [M(^{37}Cl) + H]$^+$, exact mass 633.37 for $C_{28}H_{21}Cl_4N_5O_2S$; elemental analysis: C, 53.10; H, 3.34; N, 11.06; found C, 53.11; H, 3.35; N, 11.07.

3.3.4 (1′S,2′S,3R)-5-Fluoro-2′-(5-methyl-1-(2,4,6-tri-chlorophenyl)-1*H*-1,2,3-triazole-4-carbonyl)-1′-(thiophen-2-yl)-1′,2′,5′,6′,7′,7a′-hexahydrospiro[indoline-3,3′-pyrrolizin]-2-one 4d.

The chalcone **1c** (198.5 mg, 0.5 mmol), 5-F-isatin **2b** (82.5 mg, 0.5 mmol) was used according to the general

procedure GP2 to afford the spirooxindoles triazole hybrid **4d**. m.p: 161–163 °C; white powder; 86% yield. $[\alpha]_{25}^{\lambda}$ = +118.94 (c 0.01, MeOH); (TLC: 50% *n*-hexane/EtOAc; R_f = 0.5); ^{1}H NMR (500 MHz, DMSO-d_6) δ 10.28 (s, 1H), 7.99 (s, 1H), 7.32 (dd, *J* = 5.1, 1.2 Hz, 1H), 7.01–6.80 (m, 2H), 6.48 (dd, *J* = 8.4, 4.5 Hz, 1H), 4.86 (d, *J* = 10.8 Hz, 1H), 4.11 (t, *J* = 10.4 Hz, 1H), 4.03 (ddd, *J* = 10.2, 6.7, 4.3 Hz, 1H), 3.25 (d, *J* = 7.7 Hz, 2H), 2.75 (td, *J* = 8.8, 6.4 Hz, 1H), 2.41 (s, 1H), 2.32 (ddd, *J* = 8.8, 6.8, 3.3 Hz, 1H), 1.92 (s, 2H), 1.97–1.83 (m, 3H), 1.71 (s, 1H), 1.81–1.61 (m, 1H).; ^{13}C NMR (126 MHz, DMSO-d_6) δ 192.28, 179.57, 157.59, 143.68, 142.60, 140.24, 139.44, 138.09, 134.51, 134.12, 129.92, 129.33, 127.68, 126.96, 125.30, 124.91, 116.20, 114.90, 110.71, 72.31, 71.24, 66.45, 48.47, 46.10, 28.60, 26.21, 8.29. LC/MS (ESI, *m/z*): found 618.12 [M(^{35}Cl) + H]$^+$, exact mass 616.92 for $C_{28}H_{21}Cl_3$-FN_5O_2S; elemental analysis: C, 54.51; H, 3.43; N, 11.35; found C, 54.49; H, 3.42; N, 11.37.

3.3.5 (1′S,2′S,3R)-5-Bromo-2′-(5-methyl-1-(2,4,6-tri-chlorophenyl)-1*H*-1,2,3-triazole-4-carbonyl)-1′-(thiophen-2-yl)-1′,2′,5′,6′,7′,7a′-hexahydrospiro[indoline-3,3′-pyrrolizin]-2-one 4e.

The chalcone **1c** (198.5 mg, 0.5 mmol), 5-Br-isatin **2c** (113 mg, 0.5 mmol) was used according to the general procedure GP2 to afford the spirooxindoles triazole hybrid **4e**. m.p: 158–160 °C; white powder; 88% yield. $[\alpha]_{25}^{\lambda}$ = +48.518 (c 0.01, MeOH); (TLC: 50% *n*-hexane/EtOAc; R_f = 0.675); ^{1}H NMR (600 MHz, DMSO-d_6) δ 10.50 (s, 1H), 8.02–7.97 (m, 1H), 7.35 (dd, *J* = 5.1, 1.2 Hz, 1H), 7.19 (dd, *J* = 8.3, 2.0 Hz, 1H), 7.09 (d, *J* = 2.1 Hz, 1H), 7.01 (dd, *J* = 3.6, 1.2 Hz, 1H), 6.95 (dd, *J* = 5.1, 3.4 Hz, 1H), 6.52 (d, *J* = 8.3 Hz, 1H), 4.87 (d, *J* = 10.2 Hz, 1H), 4.16–4.06 (m, 2H), 2.83–2.78 (m, 1H), 2.37–2.32 (m, 2H), 2.03 (s, 3H), 1.93 (tq, *J* = 11.5, 4.6, 3.5 Hz, 2H), 1.80–1.67 (m, 2H); ^{13}C NMR (151 MHz, DMSO-d_6) δ 192.57, 179.31, 143.69, 142.64, 142.61, 140.45, 138.17, 134.56, 134.18, 132.65, 129.96, 129.88, 129.75, 129.29, 127.85, 127.76, 125.37, 124.97, 112.93, 112.10, 71.77, 71.01, 66.28, 48.71, 46.03, 28.21, 25.87, 8.46. LC/MS (ESI, *m/z*): found 676.07 [M(^{35}Cl/^{79}Br) + H]$^+$, 778.02 [M(^{37}Cl/^{79}Br) + H]$^+$, exact mass 677.82 for $C_{28}H_{21}BrCl_3N_5O_2S$; elemental analysis: C, 49.62; H, 3.12; N, 10.33; found C, 49.62; H, 3.10; N, 10.31.

3.3.6 (1′S,2′S,3R)-1′-(Benzo[*b*]thiophen-2-yl)-5-fluoro-2′-(5-methyl-1-(2,4,6-trichlorophenyl)-1*H*-1,2,3-triazole-4-carbonyl)-1′,2′,5′,6′,7′,7a′-hexahydrospiro[indoline-3,3′-pyrrolizin]-2-one 4f.

The chalcone **1b** (223.5 mg, 0.5 mmol), 5-F-isatin **2b** (82.5 mg, 0.5 mmol) was used according to the general procedure GP2 to afford the spirooxindoles triazole hybrid **4f**. m.p: 163–165 °C; white powder; 84% yield. $[\alpha]_{25}^{\lambda}$ = +43.648 (c 0.01, MeOH); (TLC: 50% *n*-hexane/EtOAc; R_f = 0.55); ^{1}H NMR (600 MHz, CDCl$_3$) δ 8.34 (s, 1H), 7.76 (d, *J* = 7.8 Hz, 1H), 7.69 (d, *J* = 7.6 Hz, 1H), 7.45 (dd, *J* = 5.9, 3.7 Hz, 2H), 7.35 (d, *J* = 4.2 Hz, 1H), 7.33–7.21 (m, 1H), 6.86 (d, *J* = 8.0 Hz, 1H), 6.74 (td, *J* = 8.7, 2.8 Hz, 1H), 6.62 (dd, *J* = 8.6, 4.3 Hz, 1H), 5.29–5.22 (m, 1H), 5.25 (s, 1H), 4.49 (ddd, *J* = 10.8, 7.0, 4.0 Hz, 1H), 4.26 (t, *J* = 10.4 Hz, 1H), 2.95–2.89 (m, 1H), 2.72–2.65 (m, 1H), 2.13 (d, *J* = 4.2 Hz, 3H), 2.01 (dp, *J* = 11.6, 4.4, 3.4 Hz, 2H), 1.97–1.84 (m, 2H); ^{13}C NMR (151 MHz, DMSO-d_6) δ 192.21, 179.60, 157.64 (d, *J* = 236.9 Hz), 144.80, 142.57, 140.36, 140.05, 139.53, 138.96, 138.13, 134.53, 134.14, 129.93, 129.34, 126.97, 124.99, 124.56, 123.71, 122.92, 122.00, 116.30, 114.92, 110.84, 72.41, 70.83, 66.05, 48.57, 46.88, 28.60, 26.20, 8.34. LC/MS (ESI, *m/z*): found 666.14

$[M(^{35}Cl) + H]^+$, exact mass 666.98 for $C_{32}H_{23}Cl_3FN_5O_2S$; elemental analysis: C, 57.63; H, 3.48; N, 10.50; found C, 57.62; H, 3.49; N, 10.53.

3.3.7 (1′S,2′S,3R)-1′-(Benzofuran-2-yl)-5-fluoro-2′-(5-methyl-1-(2,4,6-trichlorophenyl)-1H-1,2,3-triazole-4-carbonyl)-1′,2′,5′,6′,7′,7a′-hexahydrospiro[indoline-3,3′-pyrrolizin]-2-one 4g.

The chalcone **1a** (215.5 mg, 0.5 mmol), 5-F-isatin **2b** (82.5 mg, 0.5 mmol) was used according to the general procedure GP2 to afford the spirooxindoles triazole hybrid **4g**. m.p: 165–167 °C; brown powder; 81% yield. $[\alpha]_{25}^{\lambda} = +14.915$ (c 0.01, MeOH); (TLC: 50% n-hexane/EtOAc; $R_f = 0.525$); ^{1}H NMR (600 MHz, CDCl₃) δ 8.77 (s, 1H), 7.48 (dd, J = 7.9, 3.2 Hz, 1H), 7.44 (dt, J = 11.2, 2.4 Hz, 3H), 7.27–7.13 (m, 2H), 6.85 (dd, J = 8.2, 2.7 Hz, 1H), 6.74 (td, J = 8.8, 4.4 Hz, 1H), 6.71–6.63 (m, 2H), 5.39 (dd, J = 10.9, 2.5 Hz, 1H), 4.60–4.52 (m, 1H), 4.18 (td, J = 10.5, 2.7 Hz, 1H), 2.92 (q, J = 8.0 Hz, 1H), 2.77–2.70 (m, 1H), 2.17 (dd, J = 7.5, 4.1 Hz, 1H), 2.11 (s, 3H), 2.05–1.91 (m, 3H). ^{13}C NMR (151 MHz, CDCl₃) δ 191.99, 179.95, 158.92, 158.12–153.90, 142.45, 140.06, 138.31, 138.13, 135.17, 134.75, 129.52, 129.03, 128.69, 126.81, 123.74, 122.70, 120.63, 115.98, 114.59, 111.35, 110.96, 103.53, 72.48, 68.45, 62.44, 48.66, 44.93, 29.80, 28.97, 25.91, 8.57. LC/MS (ESI, m/z): found 652.14 $[M(^{35}Cl) + H]^+$, exact mass 650.92 for $C_{32}H_{23}Cl_3FN_5O_3$; elemental analysis: C, 59.05; H, 3.56; N, 10.76; found C, 59.04; H, 3.55; N, 10.74.

3.3.8 (1′S,2′S,3R)-1′-(Benzofuran-2-yl)-5-bromo-2′-(5-methyl-1-(2,4,6-trichlorophenyl)-1H-1,2,3-triazole-4-carbonyl)-1′,2′,5′,6′,7′,7a′-hexahydrospiro[indoline-3,3′-pyrrolizin]-2-one 4h.

The chalcone **1a** (215.5 mg, 0.5 mmol), 5-Br-isatin **2c** (113 mg, 0.5 mmol) was used according to the general procedure GP2 to afford the spirooxindoles triazole hybrid **4h**. m.p: 170–172 °C; yellow powder; 83% yield. $[\alpha]_{25}^{\lambda} = +25.227$ (c 0.01, MeOH); (TLC: 50% n-hexane/EtOAc; $R_f = 0.65$); ^{1}H NMR (600 MHz, CDCl₃) δ 8.77 (s, 1H), 7.48 (dd, J = 7.9, 3.2 Hz, 1H), 7.44 (dt, J = 11.2, 2.4 Hz, 3H), 7.27–7.13 (m, 2H), 6.85 (dd, J = 8.2, 2.7 Hz, 1H), 6.74 (td, J = 8.8, 4.4 Hz, 1H), 6.71–6.63 (m, 2H), 5.39 (dd, J = 10.9, 2.5 Hz, 1H), 4.60–4.52 (m, 1H), 4.18 (td, J = 10.5, 2.7 Hz, 1H), 2.92 (q, J = 8.0 Hz, 1H), 2.77–2.70 (m, 1H), 2.17 (dd, J = 7.5, 4.1 Hz, 1H), 2.11 (s, 3H), 2.05–1.91 (m, 3H). ^{13}C NMR (151 MHz, CDCl₃) δ 191.99, 179.95, 158.92, 158.12–153.90, 142.45, 140.06, 138.31, 138.13, 135.17, 134.75, 129.52, 129.03, 128.69, 126.81, 123.74, 122.70, 120.63, 115.98, 114.59, 111.35, 110.96, 103.53, 72.48, 68.45, 62.44, 48.66, 44.93, 29.80, 28.97, 25.91, 8.57. LC/MS (ESI, m/z): found 710.12 $[M(^{35}Cl/^{79}Br) + H]^+$, 714.10 $[M(^{37}Cl/^{79}Br) + H]^+$, exact mass 711.82 for $C_{32}H_{23}Cl_4N_5O_3$; elemental analysis: C, 54.00; H, 3.26; N, 9.84; found: C, 54.01; H, 3.27; N, 9.85.

3.3.9 (1′S,2′S,3R)-5-Chloro-2′-(5-methyl-1-(2,4,6-trichlorophenyl)-1H-1,2,3-triazole-4-carbonyl)-1′-(thiophen-2-yl)-1′,2′,5′,6′,7′,7a′-hexahydrospiro[indoline-3,3′-pyrrolizin]-2-one 4i.

The chalcone **1c** (198.5 mg, 0.5 mmol), 5-Cl-isatin **2d** (90.5 mg, 0.5 mmol) was used according to the general procedure GP2 to afford the spirooxindoles triazole hybrid **4i**. m.p: 152–154 °C; yellow crystals; 89% yield. $[\alpha]_{25}^{\lambda} = +40.638$ (c 0.01, MeOH); (TLC: 50% n-hexane/EtOAc; $R_f = 0.6$); ^{1}H NMR (600 MHz, DMSO-d₆) δ 10.48 (s, 1H), 8.01 (d, J = 2.3 Hz, 2H), 7.36 (dd, J = 5.1, 1.2 Hz, 1H), 7.08 (dd, J = 8.3, 2.1 Hz, 1H), 7.04–6.98 (m, 2H), 6.96 (dd, J = 5.1, 3.4 Hz, 1H), 6.56 (d, J = 8.3 Hz, 1H), 4.88

(d, J = 10.5 Hz, 1H), 4.14 (t, J = 10.3 Hz, 1H), 4.09 (ddd, J = 10.4, 6.9, 4.0 Hz, 1H), 2.46 (d, J = 3.8 Hz, 2H), 2.01 (s, 3H), 1.94 (dddd, J = 15.1, 13.4, 7.5, 3.7 Hz, 2H), 1.81–1.67 (m, 2H);^{13}C NMR (151 MHz, DMSO-d₆) δ 192.50, 179.38, 143.69, 142.63, 142.25, 140.40, 138.15, 134.55, 134.17, 129.98, 129.91, 129.79, 129.32, 127.73, 127.45, 127.09, 125.36, 125.32, 124.97, 111.54, 71.88, 71.08, 66.33, 48.66, 46.06, 28.32, 25.98, 8.39. LC/MS (ESI, m/z): found 632.09 $[M(^{35}Cl) + H]^+$, 634.12 $[M(^{37}Cl) + H]^+$, exact mass 633.37 for $C_{28}H_{21}Cl_4N_5O_2S$; elemental analysis: C, 53.10; H, 3.34; N, 11.06; found C, 53.11; H, 3.34; N, 11.04.

3.3.10 (1′S,2′S,3R)-1′-(Furan-2-yl)-5-methyl-2′-(5-methyl-1-(2,4,6-trichlorophenyl)-1H-1,2,3-triazole-4-carbonyl)-1′,2′,5′,6′,7′,7a′-hexahydrospiro[indoline-3,3′-pyrrolizin]-2-one 4j.

The chalcone **1d** (190.5 mg, 0.5 mmol), 5-Me-isatin **2e** (80.5 mg, 0.5 mmol) was used according to the general procedure GP2 to afford the spirooxindoles triazole hybrid **4j**. m.p: 193–195 °C; brown powder; 86% yield. $[\alpha]_{25}^{\lambda} = +48.228$ (c 0.01, MeOH); (TLC: 50% n-hexane/EtOAc; $R_f = 0.45$); ^{1}H NMR (600 MHz, DMSO-d₆) δ 10.17 (d, J = 8.0 Hz, 1H), 8.04–7.98 (m, 2H), 7.55 (d, J = 7.7 Hz, 1H), 6.80 (d, J = 7.8 Hz, 2H), 6.44–6.34 (m, 2H), 6.27–6.21 (m, 1H), 4.95 (d, J = 9.9 Hz, 1H), 4.10 (ddt, J = 10.6, 7.0, 4.4 Hz, 1H), 3.98–3.91 (m, 2H), 2.10 (d, J = 8.0 Hz, 3H), 1.99 (dq, J = 8.2, 3.8 Hz, 1H), 1.96 (d, J = 8.2 Hz, 4H), 1.89 (t, J = 6.5 Hz, 1H), 1.79 (ddd, J = 12.5, 8.2, 4.1 Hz, 1H), 1.69 (dd, J = 12.0, 8.2 Hz, 1H). ^{13}C NMR (151 MHz, DMSO-d₆) δ 192.73, 179.63, 154.40, 142.77, 142.70, 140.84, 140.13, 138.06, 134.73, 134.15, 130.10, 129.92, 129.47, 127.93, 125.60, 111.04, 109.78, 106.35, 71.82, 68.03, 62.40, 48.66, 44.33, 28.61, 25.77, 21.09, 8.32. LC/MS (ESI, m/z): found 596.15 $[M(^{35}Cl) + H]^+$, exact mass 595.09 for $C_{29}H_{24}Cl_3N_5O_3$; elemental analysis: C, 58.36; H, 4.05; N, 11.73; found C, 58.37; H, 4.06; N, 11.75.

3.3.11 (1′S,2′S,3R)-5-Methyl-2′-(5-methyl-1-(2,4,6-trichlorophenyl)-1H-1,2,3-triazole-4-carbonyl)-1′-(thiophen-2-yl)-1′,2′,5′,6′,7′,7a′-hexahydrospiro[indoline-3,3′-pyrrolizin]-2-one 4k.

The chalcone **1c** (198.5 mg, 0.5 mmol), 5-Me-isatin **2e** (80.5 mg, 0.5 mmol) was used according to the general procedure GP2 to afford the spirooxindoles triazole hybrid **4h**. m.p: 197–199 °C; brown powder; 80% yield. $[\alpha]_{25}^{\lambda} = +55.820$ (c 0.01, MeOH); (TLC: 50% n-hexane/EtOAc; $R_f = 0.5$); ^{1}H NMR (400 MHz, DMSO-d₆) δ 10.20 (d, J = 2.8 Hz, 1H), 7.99 (d, J = 3.1 Hz, 2H), 7.35 (t, J = 3.8 Hz, 1H), 7.01 (d, J = 3.4 Hz, 1H), 6.96 (dd, J = 5.8, 2.7 Hz, 1H), 6.83–6.77 (m, 2H), 6.42 (dd, J = 7.8, 3.1 Hz, 1H), 4.90–4.85 (m, 1H), 4.14–4.09 (m, 2H), 2.88–2.81 (m, 1H), 2.37–2.28 (m, 2H), 2.10 (d, J = 3.0 Hz, 3H), 1.98–1.88 (m, 4H), 1.80–1.63 (m, 2H), 1.58–1.54 (m, 1H). ^{13}C NMR (151 MHz, DMSO-d₆) δ 192.76, 179.65, 144.00, 142.80, 140.84, 140.13, 138.07, 134.70, 134.15, 130.10, 130.00, 129.90, 129.85, 129.43, 127.90, 127.72, 127.14, 125.50, 125.26, 124.88, 109.83, 72.04, 70.94, 66.16, 48.82, 46.20, 28.43, 25.75, 21.09, 8.95, 8.30. LC/MS (ESI, m/z): found 612.14 $[M(^{35}Cl) + H]^+$, exact mass 612.95 for $C_{29}H_{24}Cl_3N_5O_3S$; elemental analysis: C, 56.83; H, 3.95; N, 11.43; found C, 56.85; H, 3.94; N, 11.41.

3.4 X-ray structure determination

The crystals of **acetyl-triazole derivative, 1a**, and **1b** were immersed in cryo-oil, mounted in a loop, and measured at a temperature of 120–121 K. The X-ray diffraction data were

collected on a Rigaku Oxford Diffraction Supernova diffractometer using Cu Kα radiation (**acetyl-triazole derivative** and **1b**) or Mo Kα radiation (**1a**). The CrysAlisPro[40] software package was used for cell refinements and data reductions. A multi-scan (**acetyl-triazole derivative** and **1a**) or an analytical (**1b**) absorption correction (CrysAlisPro[40]) was applied to the intensities before the structure solutions. The structures were solved by the intrinsic phasing (SHELXT[41]) method. Structural refinements were carried out using SHELXL[42] software with SHELXLE[43] graphical user interface. All hydrogen atoms were positioned geometrically and constrained to ride on their parent atoms, with C–H = 0.95–0.99 Å and U_{iso} = 1.2–1.5 U_{eq}(parent atom). The crystallographic details are summarized in Table S1.†

3.5 Biological investigations

3.5.1 Cytotoxic activity. HepG2 cancer and THLE2 normal cells were purchased from the "National Cancer Institute in Cairo, Egypt", and were cultured in "RPMI-1640 medium L-glutamine (Lonza Verviers SPRL, Belgium, cat#12-604F). The cells were cultured in 10% fetal bovine serum (FBS, Sigma-Aldrich, MO, USA) and 1% penicillin–streptomycin (Lonza, Belgium)". All cells were incubated at 37 °C in 5% carbon dioxide atmosphere (NuAire) following standard tissue culture work. In a 96-well plate, cells were plated in triplicate at a density of 5×10^4 cells and were treated with the compounds at concentrations of "0.01, 0.1, 1, 10, and 100 μM" on the second day. Cell viability was assessed using MTT solution (Promega, USA) following routine work.[44] The viability was calculated in comparison to the control, and the IC_{50} values were computed.[45]

3.5.2 EGFR/PARP-1 enzyme inhibition. EGFR-TK assay kit "ADP-Glo™ kinase assay, Cat No. V9261, Promega, USA" and PARP-1 assay kit "Bioscience, Cat No. 80580, CA, USA" were performed to evaluate the inhibitory potency of compounds **4a**, **4b** and **4f** against the EGFR and PARP-1. The autophosphorylation percentage inhibition by compounds was calculated using the following equation: $100 - \left[\dfrac{\text{control}}{\text{treated}} - \text{control}\right]$ using the curves of percentage inhibition of eight concentrations of each compound, IC_{50} was calculated using the GraphPad prism7 software.[46,47]

3.6 Flow cytometry using Annexin V/PI staining

HepG2 cells were seeded into 6-well culture plates ($3–5 \times 10^5$ cells per well) and incubated overnight. Cells were then treated for 48 h with **4a** at their IC_{50} values. Next, media supernatants and cells were collected and rinsed with ice-cold PBS. The cells were then suspended in 100 μL of annexin binding buffer solution "25 mM $CaCl_2$, 1.4 M NaCl, and 0.1 M Hepes/NaOH, pH 7.4" and incubated with "Annexin V-FITC solution (1 : 100) and propidium iodide (PI)" at a concentration equal to 10 μg mL^{-1} in the dark for 30 min. Stained cells were then acquired using a Cytoflex flow cytometer (Beckman Coulter C02946) machine. Data were analyzed using Fowjo v10.1 Software (BD life sciences).[45,48]

3.6.1 Gene expression analysis using RT-PCR. To further investigate the apoptotic pathway, we assessed the gene expression of "P53, Bax, caspases-3,8,9 as proapoptotic genes, and BCL-2 as the anti-apoptotic gene". HepG2 cells were treated with compound **4a** at its IC_{50} value for 48 h. After completing the treatment period, cells were collected, and total RNA was extracted using Rneasy® Mini Kit (Qiagen, Hilden, Germany). Then, cDNA was synthesized using 500 ng of RNA (i-Script cDNA synthesis kit, BioRad, Hercules, USA). Finally, each RT-PCR reaction was performed following routine work. Then, the Ct values were collected to calculate the relative genes' expression in fold-change for all samples by normalization to the "β-actin housekeeping gene".[49,50]

3.6.2 Molecular docking. Molecular docking studies were performed to evaluate the binding modes of spirotriazole derivatives against poly(ADP-ribose)polymerase (PARP1) and Epidermal Growth Factor Receptor (EGFR). For this purpose, the crystal structure of PDB IDs 7AAD[51] and 1M17,[52] respectively, were downloaded from the Research Collaboratory for Structural Bioinformatics Protein Data Bank (RCSB PDB). The downloaded protein structures were checked for any missing residues, which were then corrected along with bond order, while formal charges were assessed and fixed. The structures of spirotriazole derivatives were created using the builder module, and the charges on compounds were minimized using the Merck Molecular Force Field 94x. These compounds were then subjected to molecular docking with the already prepared protein structures with the help of Molecular Operating Environment (MOE)[53] software.

For the purpose of molecular docking, Triangle Matcher method was used as the primary placement method for docking, while LondondG was implemented as the placement scoring method. 'Induced fit receptor' algorithm was used for the refinement of the 50 generated poses, out of which, top 10 poses scored via GBVI/WSA dG method were used for further analysis. The binding poses of the top-ranked compounds were then analysed using Protein–Ligand Interaction Profiler (PLIP)[54] to visualize, identify, and further analyze protein–ligand interactions. PLIP serves to validate the docking results and allow in-depth study of the protein–ligand interactions, and to visualize the structures and interactions. The 3D interaction figures were made with the help of Chimera.

3.6.3 Molecular simulation. The protein–ligand complex with the best IC_{50} and top-ranked pose was further subjected to Molecular Dynamics Simulation spanning 50 nanosecond utilizing CHARMM36m Forcefields[55] while the general Amber force field (GAFF)[56] was used to parameterize the ligands. The systems were first subjected to steepest descent energy minimization comprising 2500 steps followed by conjugate gradient minimization.[57] The position restraints were used to hold the protein fixed and the process was repeated multiple times (6×) with gradual decrease in applied restrain. Finally, the applied restrain was lifted and systems were subjected to another round of energy minimization. The systems were then heated for a period of 500 ps to the target temperature of 300 K under a constant volume, temperature (NVT) ensemble. The process was repeated twice with a gradual decrease in positional restraints from 30 to 10 kcal mol. In subsequent steps, the equilibration was carried out at a constant pressure and

temperature (NPT) ensemble for a period of approximately 3.5 ns. Lastly, 50 ns of the production run was performed under periodic boundary conditions. The temperature and pressure were controlled using Langevin dynamics and isotropic position scaling The Particle Mesh Ewald (PME) method was used for long-range electrostatic interactions.[58] The numerical integration was set at a time step of 2 fs. The simulated trajectories were analyzed using the CPPTRAJ[59] program and VMD. The stability metrics considered herein include root mean square deviation (RMSD), root mean square fluctuation (RMSF), and radius of gyration (R_g).

4 Conclusion

The successful synthesis and characterization of spirooxindole-triazole hybrids through [3 + 2] cycloaddition reactions have resulted in novel compounds with potent inhibitory activity against EGFR and PARP-1. These hybrids represent promising candidates for targeted cancer therapy, combining structural innovation with enhanced biological efficacy. Interestingly, Interestingly, compound 4a showed potent cytotoxicity against HepG2 cells with IC$_{50}$ values of 3.6 μM compared to doxorubicin (IC$_{50}$ = 2.78 μM), with poor cytotoxicity against THLE2 cells with IC$_{50}$ values higher than 40 μM in a selective way. It exhibited potent EGFR and PARP-1 inhibition with IC$_{50}$ values of 74.6 nM and 2.01 nM, respectively. Furthermore, compound 4a-treatment induced apoptosis by 6.6-fold, arresting the cell cycle at the G0–G1 phase. Overall, our study underscores the potent activity of compound 4a as dual EGFR/PARP-1 inhibitors against liver cancer. Further *in vivo* animal model and preclinical studies will focus on optimizing this compound for clinical application, potentially leading to new and effective treatment liver cancer.

Data availability

Data supporting this study are openly available from the corresponding author: Prof. Assem Barakat.

Author contributions

Assem Barakat, Abdulmajeed Abdullah Alayyaf and Muhanna K. Al-Muhanna: conceptualization and supervision; M. Ali, Moayad Abdullah Alwehaibi, Naif S. Almuqati, and Abdullah A. Alghamdi: investigation, methodology, and formal analysis; Matti Haukka: X-ray diffraction analysis, software; Mohamed S. Nafie: conceptualization of anticancer activity with signaling pathway and biological analysis; Syeda Sumayya Tariq, and Zaheer-Ul Haq: computational study and software; All authors contributed in writing –review & editing in their respective parts.

Conflicts of interest

There are no conflicts to declare.

References

1 J. L Arias, Drug targeting strategies in cancer treatment: an overview, *Mini-Rev. Med. Chem.*, 2011, **11**(1), 1–17.

2 S. H. Kaufmann and W. C. Earnshaw, Induction of apoptosis by cancer chemotherapy, *Exp. Cell Res.*, 2000, **256**(1), 42–49.

3 E. K. Rowinsky, Signal events: cell signal transduction and its inhibition in cancer, *Oncologist*, 2003, **8**(S3), 5–17.

4 C. Garnis, T. P. Buys and W. L. Lam, Genetic alteration and gene expression modulation during cancer progression, *Mol. Cancer*, 2004, **3**, 1–23.

5 M. H. Naseri, M. Mahdavi, J. Davoodi, S. H. Tackallou, M. Goudarzvand and S. H. Neishabouri, Up regulation of Bax and down regulation of Bcl2 during 3-NC mediated apoptosis in human cancer cells, *Cancer Cell Int.*, 2015, **15**, 1–9.

6 N. J. Curtin, PARP inhibitors for cancer therapy, *Expert Rev. Mol. Med.*, 2005, **7**(4), 1–20.

7 M. J. Schiewer and K. E. Knudsen, Transcriptional roles of PARP1 in cancer, *Mol. Cancer Res.*, 2014, **12**(8), 1069–1080.

8 M. Rose, J. T. Burgess, K. O'Byrne, D. J. Richard and E. Bolderson, PARP inhibitors: clinical relevance, mechanisms of action and tumor resistance, *Front. Cell Dev. Biol.*, 2020, **8**, 564601.

9 L. Wang, W. Cai, W. Zhang, X. Chen, W. Dong, D. Tang, Y. Zhang, C. Ji and M. Zhang, Inhibition of poly (ADP-ribose) polymerase 1 protects against acute myeloid leukemia by suppressing the myeloproliferative leukemia virus oncogene, *Oncotarget*, 2015, **6**(29), 27490.

10 K. Kondo, S. Obitsu, S. Ohta, K. Matsunami, H. Otsuka and R. Teshima, Poly (ADP-ribose) polymerase (PARP)-1-independent apoptosis-inducing factor (AIF) release and cell death are induced by eleostearic acid and blocked by α-tocopherol and MEK inhibition, *J. Biol. Chem.*, 2010, **285**(17), 13079–13091.

11 L. E. Dockery, C. C. Gunderson and K. N. Moore, Rucaparib: the past, present, and future of a newly approved PARP inhibitor for ovarian cancer, *OncoTargets Ther.*, 2017, 3029–3037.

12 S. Li, X. Y. Li, T. J. Zhang, M. O. Kamara, J. W. Liang, J. Zhu and F. H. Meng, Design, synthesis and biological evaluation of homoerythrina alkaloid derivatives bearing a triazole

moiety as PARP-1 inhibitors and as potential antitumor drugs, *Bioorg. Chem.*, 2020, **94**, 103385.

13 H. F. Ashour, L. A. Abou-Zeid, A. A. Magda and K. B. Selim, 1, 2, 3-Triazole-Chalcone hybrids: Synthesis, in vitro cytotoxic activity and mechanistic investigation of apoptosis induction in multiple myeloma RPMI-8226, *Eur. J. Med. Chem.*, 2020, **189**, 112062.

14 K. Bozorov, J. Zhao and H. A. Aisa, 1, 2, 3-Triazole-containing hybrids as leads in medicinal chemistry: A recent overview, *Bioorg. Med. Chem.*, 2019, **27**(16), 3511–3531.

15 D. Dheer, V. Singh and R. Shankar, Medicinal attributes of 1, 2, 3-triazoles: Current developments, *Bioorg. Chem.*, 2017, **71**, 30–54.

16 D. Lengerli, K. Ibis, Y. Nural and E. Banoglu, The 1, 2, 3-triazole 'all-in-one' ring system in drug discovery: A good bioisostere, a good pharmacophore, a good linker, and a versatile synthetic tool, *Expert Opin. Drug Delivery*, 2022, **17**(11), 1209–1236.

17 I. Shawish, S. Alayoubi, A. El-Faham, A. Aldalbahi, F. Elsenduny, F. Badria, M. Ríos Gutiérrez, H. Hammud, S. Ashraf, Z. Ul-Haq and A. Barakat, Novel Spirooxindole-Triazole Derivatives: Unveiling [3+2] Cycloaddition Reactivity Through Molecular Electron Density Theory and Investigating Their Potential Cytotoxicity Against HepG2 and MDA-MB-231 Cell Lines, *Front. Chem.*, 2024, **12**, 1460384, DOI: 10.3389/fchem.2024.1460384.

18 S. Li, X. Y. Li, T. J. Zhang, J. Zhu, W. H. Xue, X. H. Qian and F. H. Meng, Design, synthesis and biological evaluation of erythrina derivatives bearing a 1, 2, 3-triazole moiety as PARP-1 inhibitors, *Bioorg. Chem.*, 2020, **96**, 103575.

19 S. G. Agalave, S. R. Maujan and V. S. Pore, Click chemistry: 1, 2, 3-triazoles as pharmacophores, *Chem.–Asian J.*, 2011, **6**(10), 2696–2718.

20 N. Normanno, A. De Luca, C. Bianco, L. Strizzi, M. Mancino, M. R. Maiello, A. Carotenuto, G. De Feo, F. Caponigro and D. S. Salomon, Epidermal growth factor receptor (EGFR) signaling in cancer, *Gene*, 2006, **366**(1), 2–16.

21 W. M. Eldehna, D. H. El-Naggar, A. R. Hamed, H. S. Ibrahim, H. A. Ghabbour and H. A. Abdel-Aziz, One-pot three-component synthesis of novel spirooxindoles with potential cytotoxic activity against triple-negative breast cancer MDA-MB-231 cells, *J. Enzyme Inhib. Med. Chem.*, 2018, **33**(1), 309–318.

22 R. M. Al-Jassas, M. S. Islam, A. M. Al-Majid, M. S. Nafie, M. Haukka, A. M. Rahman, A. M. A. Alayyaf and A. Barakat, Synthesis and SARs study of novel spiro-oxindoles as potent antiproliferative agents with CDK-2 inhibitory activities, *Arch. Pharm.*, 2023, **356**(8), 2300185.

23 M. S. Nafie, A. M. Al-Majid, M. Ali, A. A. Alayyaf, M. Haukka, S. Ashraf, Z. Ul-Haq, A. El-Faham and A. Barakat, Exploring pyrrolidinyl-spirooxindole natural products as promising platforms for the synthesis of novel spirooxindoles as EGFR/CDK2 inhibitors for halting breast cancer cells, *Front. Chem.*, 2024, **12**, 1364378.

24 P. V. Chavan, U. V. Desai, P. P. Wadgaonkar, S. R. Tapase, K. M. Kodam, A. Choudhari and D. Sarkar, Click chemistry based multicomponent approach in the synthesis of spirochromenocarbazole tethered 1, 2, 3-triazoles as potential anti-cancer agents, *Bioorg. Chem.*, 2019, **85**, 475–486.

25 A. Barakat, S. Alshahrani, A. M. Al-Majid, A. S. Alamary, M. Haukka, M. M. Abu-Serie, L. R. Domingo, S. Ashraf, Z. Ul-Haq, M. S. Nafie and M. Teleb, New spiro-indeno [1, 2-b] quinoxalines clubbed with benzimidazole scaffold as CDK2 inhibitors for halting non-small cell lung cancer; stereoselective synthesis, molecular dynamics and structural insights, *J. Enzyme Inhib. Med. Chem.*, 2023, **38**(1), 2281260.

26 S. Alshahrani, A. M. Al-Majid, A. S. Alamary, M. Ali, M. S. Altowyan, M. Ríos-Gutiérrez, S. Yousuf and A. Barakat, Synthesis and Characterization of New Spirooxindoles Including Triazole and Benzimidazole Pharmacophores *via* [3+2] Cycloaddition Reaction: An MEDT Study of the Mechanism and Selectivity, *Molecules*, 2023, **28**(19), 6976.

27 A. Barakat, S. Alshahrani, A. M. Al-Majid, A. S. Alamary, M. Haukka, M. M. Abu-Serie, A. Dömling, L. R. Domingo and Y. A. Elshaier, Activation of p53 signaling and regression of breast and prostate carcinoma cells by spirooxindole-benzimidazole small molecules, *Front. Pharmacol.*, 2024, **15**, 1358089.

28 M. Ali, M. A. Alwehaibi, A. M. Al-Majid, M. K. Al-Muhanna, S. M. Soliman, M. Ríos-Gutiérrez, M. Haukka, A. A. Alayyaf, A. Barakat, *CCDC 2303110: Experimental Crystal Structure Determination*, CSD Communication, 2024, DOI: 10.5517/ccdc.csd.cc2h9kw8.

29 M. Ali, M. A. Alwehaibi, A. M. Al-Majid, M. K. Al-Muhanna, S. M. Soliman, M. Ríos-Gutiérrez, M. Haukka, A. A. Alayyaf, A. Barakat, *CCDC 2303111: Experimental Crystal Structure Determination*, CSD Communication, 2024, DOI: 10.5517/ccdc.csd.cc2h9kx9.

30 C. Schettino, M. A. Bareschino, V. Ricci and F. Ciardiello, Erlotinib: an EGF receptor tyrosine kinase inhibitor in non-small-cell lung cancer treatment, *Expert Rev. Respir. Med.*, 2008, **2**(2), 167–178.

31 C. C. Gunderson and K. N. Moore, Olaparib: an oral PARP-1 and PARP-2 inhibitor with promising activity in ovarian cancer, *Future Oncol.*, 2015, **11**(5), 747–757.

32 K. R. Senwar, P. Sharma, T. S. Reddy, M. K. Jeengar, V. L. Nayak, V. G. M. Naidu, A. Kamal and N. Shankaraiah, Spirooxindole-derived morpholine-fused-1, 2, 3-triazoles: Design, synthesis, cytotoxicity and apoptosis inducing studies, *Eur. J. Med. Chem.*, 2015, **102**, 413–424.

33 M. Rajeswari, S. Kumari and J. M. Khurana, One-pot four component domino strategy for the synthesis of novel spirooxindole pyrrolizine linked 1, 2, 3-triazoles via stereo- and regioselective [3+ 2] cycloaddition reaction in acidic medium, *RSC Adv.*, 2016, **6**(11), 9297–9303.

34 R. Bianco, T. Gelardi, V. Damiano, F. Ciardiello and G. Tortora, Rational bases for the development of EGFR inhibitors for cancer treatment, *Int. J. Biochem. Cell Biol.*, 2007, **39**(7–8), 1416–1431.

35 T. I. Adelusi, A. Q. K. Oyedele, I. D. Boyenle, A. T. Ogunlana, R. O. Adeyemi, C. D. Ukachi, M. O. Idris, O. T. Olaoba, I. O. Adedotun, O. E. Kolawole and Y. Xiaoxing, Molecular modeling in drug discovery, *Inform. Med. Unlocked*, 2022, **29**, 100880.

36 M. A. Ashiru, S. O. Ogunyemi, O. R. Temionu, A. C. Ajibare, N. C. Cicero-Mfon, O. A. Ihekuna, M. O. Jagun, L. Abdulmumin, Q. K. Adisa, Y. E. Asibor and C. J. Okorie, Identification of EGFR inhibitors as potential agents for cancer therapy: pharmacophore-based modeling, molecular docking, and molecular dynamics investigations, *Mol. Model.*, 2023, **29**(5), 128.

37 K. H. Liao, K. B. Chen, W. Y. Lee, M. F. Sun, C. C. Lee and C. Y. C. Chen, Ligand-Based and Structure-Based Investigation for Alzheimer's Disease from Traditional Chinese Medicine, *J. Evidence-Based Complementary Altern. Med.*, 2014, **2014**(1), 364819.

38 T. E. Ogden, J. C. Yang, M. Schimpl, L. E. Easton, E. Underwood, P. B. Rawlins, M. M. McCauley, M. F. Langelier, J. M. Pascal, K. J. Embrey and D. Neuhaus, Dynamics of the HD regulatory subdomain of PARP-1; substrate access and allostery in PARP activation and inhibition, *Nucleic Acids Res.*, 2021, **49**(4), 2266–2288.

39 A. A. Alayyaf, M. Ali, M. A. Alwehaibi, M. K. Al-Muhanna, S. M. Soliman, M. Ríos-Gutiérrez, M. Haukka and A. Barakat, Utilizing MEDT analysis of [3+ 2] cycloaddition reaction: x-ray crystallography of spirooxindole linked with thiophene/furan heterocycles and triazole framework, *BMC Chem.*, 2024, **18**(1), 1–16.

40 *Rikagu Oxford Diffraction, CrysAlisPro 1.171.43.100a*, Rikagu Oxford Diffraction inc., Yarnton, Oxfordshire, England, 2023.

41 G. M. Sheldrick, SHELXT – Integrated space-group and crystal-structure determination, *Acta Cryst.*, 2015, **A71**, 3–8.

42 G. M. Sheldrick, Crystal structure refinement with SHELXL, *Acta Cryst.*, 2015, **C71**, 3–8.

43 C. B. Hübschle, G. M. Sheldrick and B. Dittrich, ShelXle: a Qt graphical user interface for SHELXL, *J. Appl. Crystallogr.*, 2011, **44**, 1281–1284.

44 T. Mosmann, Rapid colorimetric assay for cellular growth and survival: application to proliferation and cytotoxicity assays, *J. Immunol. Methods*, 1983, **65**(1–2), 55–63.

45 A. T. Boraei, E. H. Eltamany, I. A. Ali, S. M. Gebriel and M. S. Nafie, Synthesis of new substituted pyridine derivatives as potent anti-liver cancer agents through apoptosis induction: In vitro, in vivo, and in silico integrated approaches, *Bioorg. Chem.*, 2021, **111**, 104877.

46 M. Hisham, B. G. Youssif, E. E. A. Osman, A. M. Hayallah and M. Abdel-Aziz, Synthesis and biological evaluation of novel xanthine derivatives as potential apoptotic antitumor agents, *Eur. J. Med. Chem.*, 2019, **176**, 117–128.

47 I. Shawish, M. S. Nafie, A. Barakat, A. Aldalbahi, H. H. Al-Rasheed, M. Ali, W. Alshaer, M. Al Zoubi, S. Al Ayoubi, B. G. De la Torre and F. Albericio, Pyrazolyl-s-triazine with indole motif as a novel of epidermal growth factor receptor/cyclin-dependent kinase 2 dual inhibitors, *Front. Chem.*, 2022, **10**, 1078163.

48 M. S. Nafie, S. M. Kishk, S. Mahgoub and A. M. Amer, Quinoline-based thiazolidinone derivatives as potent cytotoxic and apoptosis-inducing agents through EGFR inhibition, *Chem. Biol. Drug Des.*, 2022, **99**(4), 547–560.

49 M. S. Nafie, K. Arafa, N. K. Sedky, A. A. Alakhdar and R. K. Arafa, Triaryl dicationic DNA minor-groove binders with antioxidant activity display cytotoxicity and induce apoptosis in breast cancer, *Chem.-Biol. Interact.*, 2020, **324**, 109087.

50 A. I. Khodair, M. A. Alsafi and M. S. Nafie, Synthesis, molecular modeling and anti-cancer evaluation of a series of quinazoline derivatives, *Carbohydr. Res.*, 2019, **486**, 107832.

51 J. Stamos, M. X. Sliwkowski and C. Eigenbrot, Structure of the epidermal growth factor receptor kinase domain alone and in complex with a 4-anilinoquinazoline inhibitor, *J. Biol. Chem.*, 2002, **277**(48), 46265–46272.

52 S. Vilar, G. Cozza and S. Moro, Medicinal chemistry and the molecular operating environment (MOE): application of QSAR and molecular docking to drug discovery, *Curr. Top. Med. Chem.*, 2008, **8**(18), 1555–1572.

53 S. Salentin, S. Schreiber, V. J. Haupt, M. F. Adasme and M. Schroeder, PLIP: fully automated protein–ligand interaction profiler, *Nucleic Acids Res.*, 2015, **43**(W1), W443–W447.

54 J. Huang, S. Rauscher, G. Nawrocki, T. Ran, M. Feig, B. L. De Groot, H. Grubmüller and A. D. MacKerell Jr, CHARMM36m: an improved force field for folded and intrinsically disordered proteins, *Nat. Methods*, 2017, **14**(1), 71–73.

55 J. Wang, R. M. Wolf, J. W. Caldwell, P. A. Kollman and D. A. Case, Development and testing of a general amber force field, *J. Comput. Chem.*, 2004, **25**(9), 1157–1174.

56 R. Fletcher and M. J. Powell, A rapidly convergent descent method for minimization, *Comput. J.*, 1963, **6**(2), 163–168.

57 T. Darden, D. York and L. Pedersen, Particle mesh Ewald: An N log (N) method for Ewald sums in large systems, *J. Chem. Phys.*, 1993, **98**(12), 10089–10092.

58 D. R. Roe and T. E. Cheatham III, PTRAJ and CPPTRAJ: software for processing and analysis of molecular dynamics trajectory data, *J. Chem. Theory Comput.*, 2013, **9**(7), 3084–3095.

59 W. Humphrey, A. Dalke and K. Schulten, VMD: visual molecular dynamics, *J. Mol. Graphics Modell.*, 1996, **14**(1), 33–38.